Monthly Notices
of the
ROYAL ASTRONOMICAL SOCIETY

Mon. Not. R. Astron. Soc. **414,** 2246–2264 (2011) doi:10.1111/j.1365-2966.2011.18541.x

The morphologies and masses of extremely red galaxies in the Groth Strip

A. Hempel,[1,2]★ D. Cristóbal-Hornillos,[3,4] M. Prieto,[1,2] I. Trujillo,[1,2] M. Balcells,[1,2,5] C. López-Sanjuan,[1,2,6] D. Abreu,[1,2] M. C. Eliche-Moral[7] and L. Domínguez-Palmero[1,2]

[1]*Instituto de Astrofísica de Canarias, C./Vía Láctea s/n, 38200 La Laguna, Spain*
[2]*Universidad de La Laguna, C./Francisco Sánchez s/n, 38206 La Laguna, Spain*
[3]*Instituto de Astrofísica de Andalucía (CSIC), Camino Bajo de Huetor 50, 18008 Granada, Spain*
[4]*Centro de Estudios de Física del Cosmos de Aragón, C. General Pizarro, 1-3, 44001 Teruel, Spain*
[5]*Isaac Newton Group of Telescopes, Apartado de Correos 321, E-38700 Santa Cruz de la Palma, Islas Canarias, Spain*
[6]*Laboratoire d'Astrophysique de Marseille, Pôle de l'Etoile Site de Château-Gombert 38, rue Frédéric Joliot-Curie, 13388 Marseille, France*
[7]*Departamento de Astrofísica y Ciencias de la Atmósfera, Facultad de C.C. Físicas, Universidad Complutense de Madrid, 28040 Madrid, Spain*

Accepted 2011 February 14. Received 2011 February 14; in original form 2009 November 13

ABSTRACT

We present a new catalogue of EROs from the Groth Strip and study the relation between their morphology and mass. With a selection criterion F814W$-K_s \geq 4$ and $K_s \leq 21.0$ we find 102 EROs, over a survey area of 155 arcmin^2, leading to a surface density of 0.66 arcmin^{-2}. The photometric data include U, B, $F606W$, $F814W$, J, K_s bands. Morphologies are based on a by eye classification and we distinguish between three basic classes: compact objects, targets with a disc and/or a bulge component and irregular or merger candidates. An additional group consists of the few objects which could not be classified.

The majority of our targets has either a very compact morphology (34 ± 6 per cent), or show more or less distinct disc components (43 ± 6 per cent). 14 ± 4 per cent are merger or irregulars and seven objects (approximately 9 per cent) could not be classified.

We also study the dependence of structural parameters (effective radius: $r_{\rm eff}$, Sérsic index: n) on morphological appearance. As expected, EROs that are either compact or show a distinct bulge component have smaller median effective radii (1.22 ± 0.14 kpc and 3.31 ± 0.53 kpc) than disc dominated (5.50 ± 0.51 kpc) or possible irregular galaxies or merger candidates (4.92 ± 0.14 kpc). More importantly, the Sérsic index changes from 2.30 ± 0.34 and 3.24 ± 0.55, to 1.03 ± 0.24 and 1.54 ± 0.40, respectively.

As found in previous studies, most the EROs in our sample have redshifts between $z = 1$ and 2; however, compact EROs in our sample are found at redshifts as low as $z = 0.4$ and as high as $z = 2.8$; the latter qualify as well as distant red galaxies (DRGs). Disc-like EROs are also found up to $z = 2.8$; however, those with a bulge-disc structure are only seen at $z < 1.5$.

For each of these EROs we determined the stellar mass and mean population age by fitting synthetic Bruzual (2007) spectra to the photometric spectral energy distributions, via χ^2 minimization. Mass estimates were obtained by assuming an exponentially declining star formation rate with a wide set of parameters, e.g. decay time, redshift of last star formation, metallicity and optical depth. Total stellar masses for our sample are in the range $9.1 < \log(M/{\rm M}_\odot) < 11.6$. We cannot detect significant differences between the stellar mass distribution of the morphological classes. EROs with masses of $\log(M/{\rm M}_\odot) > 11.0$ dominantly show compact morphologies, but also include a significant number of sources with a disc morphology.

Key words: galaxies: evolution – galaxies: high-redshift – galaxies: photometry – galaxies: star formation – galaxies: stellar content – galaxies: structure.

1 INTRODUCTION

It has been 20 yr since the first discovery of a population of galaxies with optical to near-infrared (NIR) colours quite different from typical field sources (Elston, Rieke & Rieke 1988, 1989; Hu &

★E-mail: ahempel@iac.es

Ridgway 1994). Usually defined by $R-K \geqq 5..7$ or $I-K \geqq 4..6$ colours (in the Vega system), extremely red galaxies are a subset of extremely red objects (EROs) and we will use this more general term throughout this paper.

As diverse as the selection criteria are the stellar populations which produce such red spectral energy distributions. Today, the classification as ERO is beyond the two *classic* galaxy types, namely old evolved galaxies with no or very limited recent star formation or dusty galaxies with star formation rates (SFR) associated with starbursts, typically with redshift between 1 and 2. The ERO population also comprises normal spiral galaxies (Gilbank et al. 2003; Yan & Thompson 2003; Moustakas et al. 2004) at slightly lower redshifts. The latter contains a large fraction of edge-on galaxies, where inclination puts a reasonable amount of dust into our line of sight and reddens the spectral energy distribution (SED). Also galaxies harbouring an active galactic nucleus (AGN, Alexander et al. 2002; Brusa et al. 2005), and starburst/AGN combinations (Afonso et al. 2001) are found among the ERO samples. In addition, several other red galaxy populations have been found, e.g. IR-detected galaxies (Yan et al. 2004), distant red galaxies (DRGs, Labbé et al. 2005; Papovich 2006) and *BzK* selected galaxies (Daddi et al. 2005; Hayashi et al. 2007).

EROs are relevant because they allow to explore the abundance of massive old ellipticals, which in turn poses a strong test for the two competing scenarios of elliptical galaxy formation: early assembly ($z_{\rm f} > 2$–3), e.g. by monolithic collapse, and passive luminosity evolution thereafter (PLE models, Tinsley & Gunn 1976; Pozzetti et al. 1996), or hierarchical merging of smaller sized objects (White & Rees 1978; Kauffmann, White & Guiderdoni 1993; Somerville, Primack & Faber 2001). Observational evidence has been found for both scenarios: several surveys have detected a deficit of ellipticals at $z > 1$, supporting the hierarchical merging models (Roche, Dunlop & Almaini 2003; Kitzbichler & White 2006), while others are consistent with PLE (Cimatti et al. 2002; Im et al. 2002; Somerville et al. 2004).

In recent years the hierarchical merging scenario in a ΛCDM universe has been established as the favoured model. Nevertheless, the vast number of different renditions leaves room for dramatically different predictions regarding critical parameters like the number density of massive galaxies at specific times (Fontana et al. 2004; Treu et al. 2005, and references therein).

As a whole, extremely red galaxies are among the more massive galaxies ($M \gtrsim 10^{11}\,{\rm M}_{\odot}$) (Glazebrook et al. 2004; González-Pérez et al. 2009) and the existence of such galaxies with evolved stellar populations at high redshifts is one of the challenges to the hierarchical galaxy formation model (White & Rees 1978; Kauffmann et al. 1993; Somerville et al. 2001). However, stellar ages do not necessarily correlate with the build-up of the galaxy mass through merging (Conselice 2006; De Lucia et al. 2006; Trujillo et al. 2006; Eliche-Moral et al. 2010).

In the local universe, masses can be determined accurately by studying the dynamical mass of galaxies and obtaining scaling relations such as the Fundamental Plane for early-type galaxies (Dressler et al. 1987; Reda, Forbes & Hau 2005; La Barbera et al. 2008) and dwarf irregulars (Vaduvescu & McCall 2008) and the Tully–Fisher relation for spiral galaxies (Tully & Fisher 1977; Kassin et al. 2007). Those relations have been used successfully out to $z \sim 1.3$, but the most active area of mass assembly, $z > 1.5$, is not accessible at current times, although first steps have been taken by e.g. Cenarro & Trujillo (2009) and Cappellari et al. (2009). At higher redshifts, the baryonic mass derived from broad-band photometry is comparable to the predictions of stellar population models, like Bruzual & Charlot (2003), Maraston (2005) and Bruzual (2007).

In this paper we present an analysis of the ERO population in the Groth Strip (Prieto et al. 2005), based on optical and NIR photometry from the Galaxy Origins and Young Assembly (GOYA) photometric survey and *Hubble Space Telescope* (*HST*) imaging. We describe the morphology, stellar masses and ages, derived from broad-band photometry. Specifically we address, first whether all EROs fit in the classic morphological types, and second whether the typical stellar mass of the ERO population changes with cosmic time, and finally, whether at a given redshift the different morphologies of the ERO population correlate with the stellar mass.

The paper is structured as follows. In Section 2 we describe briefly the data available from the GOYA Survey and the sample selection. Section 3 describes the morphological classification, and Section 4 gives an overview, how stellar masses were derived using multiband photometry. Section 5 gives details on the morphology and mass estimates for each ERO class.

All magnitudes are given in the Vega system and we assume $\Omega_{\rm M} = 0.3$, $\Omega_{\Lambda} = 0.7$ and $H_0 = 70\ {\rm km\,s^{-1}\,Mpc^{-1}}$ throughout this work.

2 DATA AND SAMPLE SELECTION

We have selected a sample of extremely red galaxies (EROs) from the GOYA Survey (Balcells et al. 2002). This is a combined $K_{\rm s}$ selected catalogue covering the Groth-Westphal strip ($\approx$155 arcmin^2) in four optical bands, *U, B, F606W* and *F814W*, as well as *J*, $K_{\rm s}$ in the NIR.

The *U* and *B* imaging were taken with the Wide Field Camera (WFC) at the prime focus of the 2.5-m Isaac Newton Telescope (INT); data reduction and catalogue generation are described in Eliche-Moral et al. (2006) and Domínguez-Palmero et al. (2008); 50 per cent detection efficiencies are 24.8 mag in *U* and 25.5 mag in *B*. The *F606W* and *F814W* data originate from the Wide Field and Planetary Camera (WFPC2) on-board *HST*, as part of the original Groth Strip Survey (Groth et al. 1994), that was later analysed for the Medium Deep Survey (MDS: see, e.g. Ratnatunga, Griffiths & Ostrander (1999), and by the Deep Extragalactic Evolutionary Probe (DEEP; see, e.g., Simard et al. 2002).

The NIR $JK_{\rm s}$ data were obtained with the 1024 $\times$ 1024 pixel INGRID camera at the Cassegrain focus of the 4.2-m William Herschel Telescope (WHT). Data processing and catalogue generation are described in Cristóbal-Hornillos et al. (2003). The 50 per cent detection efficiencies range between $K_{\rm s} = 21.2$ and 20.2 mag, depending on the seeing of the individual pointings.

The EROs selection is done by running SEXTRACTOR on the original $K_{\rm s}$-band images, and photometry on all bands, including $K_{\rm s}$, is obtained on apertures of 2.6 arcsec FWHM, in double-image mode, on the images convolved to 1.3 arcsec FWHM. All sources which were classified as stellar objects, based on stellarity greater than 0.8 (given by SEXTRACTOR) in the *I* band (*F814W*) were excluded from our sample. Fig. 1 shows the colour–magnitude diagram of the whole GOYA catalogue and the final ERO sample.

All our EROs have colours redder than $F814W - K_{\rm s} \geq 4.0$. Our initial sample contains 114 objects which we have studied by eye to exclude sources close to the edge of either the *F814W* or $K_{\rm s}$-band image where we have a lower image quality. As result we have excluded six objects from our original catalogue. Additional objects have been excluded due to their unresolved morphology (see Section 5.2).

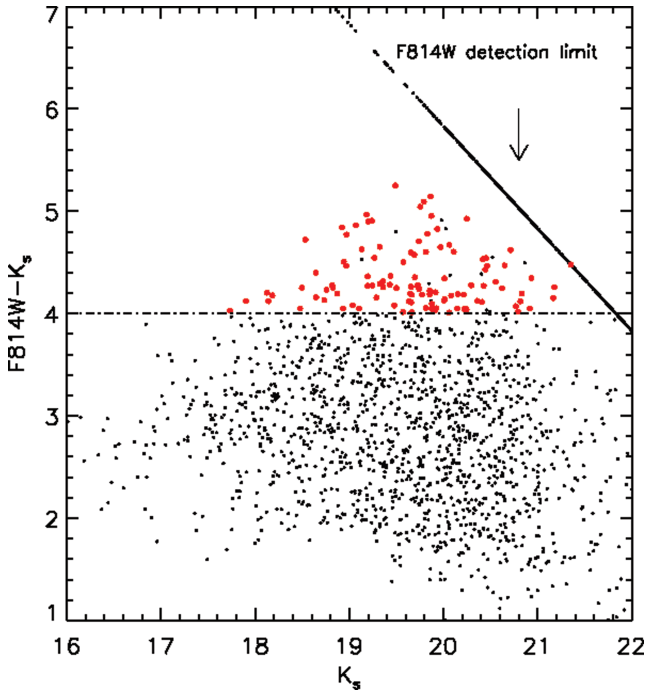

Figure 1. Colour–magnitude diagram for the full K_s selected catalogue (black) in the Groth strip and the final ERO sample (red). The horizontal line represents our colour threshold, the upper envelope is the result of the detection limit in *F814W*. Black dots above the colour threshold show objects which were excluded from our sample during the morphological classification due to their bad image quality.

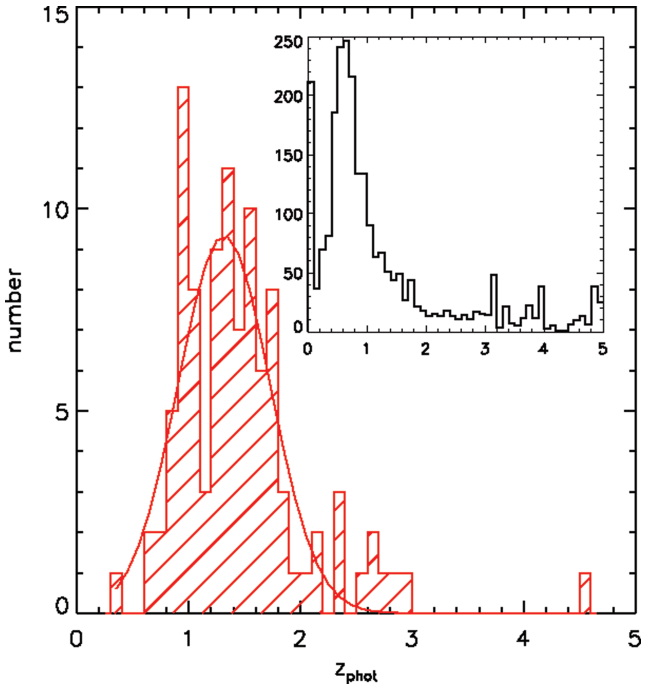

Figure 2. Histograms of the distribution of photometric redshifts, $z_{\rm phot}$, for our 102 EROs. The inset shows the result for the full K_s selected catalogue of the Groth Strip.

Several surveys have obtained spectroscopic redshifts for different galaxy populations in the Groth Strip (Weiner et al. 2005; Sarajedini et al. 2006).[1] However, the paucity of emission lines in ERO spectra, plus the lack of prominent emission lines in the visible range at redshifts above 1.4, result in very few EROs having spectroscopically determined redshifts. We therefore used photometric redshifts available from the GOYA catalogue. These were derived using *Hyperz* (Bolzonella, Miralles & Pelló 2000), redshift errors were estimated from $\sigma_{z_{\rm phot}} = \sigma_{\delta_z} \times (1 + z_{\rm phot})$ with $\sigma_{\delta_z} = 0.07$ (López-Sanjuan et al. 2009).

Based on our photo-z we can see that the used colour threshold of $F814W - K_s \geq 4$ is fairly efficient at selecting galaxies in a redshift range of $1 \leq z \leq 2$. However, this specific colour selection is not very stringent, due to the large variety of star-forming histories galaxies may have followed. Fig. 2 shows the redshift distribution of our final ERO sample, compared to the whole K-selected catalogue. As expected, most EROs have redshifts between 1 and 2, although exceptions at lower and higher redshifts exist. The redshift distribution of our ERO sample peaks at $z = 1.32 \pm 0.02$, which is in good agreement with Conselice et al. (2008) who find an average redshift for an $I - K > 4$ selected sample of $\langle z \rangle = 1.43 \pm 0.32$ (Conselice et al. 2008).

3 MORPHOLOGICAL CLASSIFICATION OF EROS

Morphologies were classified by visual inspection of the *F814W* image of each individual galaxy (Yan & Thompson 2003; Moustakas et al. 2004). Sometimes down-valued for being subjective, visual classification has a long history and is in fact the method employed to establish the morphological classification of nearby galaxies (de Vaucouleurs 1948; Ellis, Abraham & Dickinson 2001; Desai et al. 2007). We compare this visual classification with the results of a machine-based method based on fitting 2D surface-brightness Sérsic profiles (Roche et al. 2002; Simard et al. 2002; Fu, Stockton & Liu 2005; Stockton, McGrath & Canalizo 2006), using galfit (Peng et al. 2002). The later avoid human subjectivity but are also subject to limitations, e.g. when galaxy isophotes are not concentric, aligned ellipses or galaxies with large inclinations. We did not base our classification on automatic determined concentration-asymmetry indices (Abraham et al. 1996; Conselice et al. 2008; Huertas-Company et al. 2008). Concentration and asymmetry indices are difficult to interpret in EROs which tend to be compact and hence have few pixel where to measure the indices. Furthermore, important systematic errors may occur above $z \sim 1$ where the *F814W* filter samples the rest-frame UV.

Compared to both methods, a visual inspection can pick up the more subtle morphological details and the sample size is small enough to allow detailed inspection of each of the images.

With a mean redshift of 1.32 for the ERO sample, the WFPC2 data sample a rest-frame wavelength of 3500 Å and thus the *F814W* image is sensitive to star formation and to patchy dust extinction. Our morphologies may thus suffer from a 'morphological K -correction bias'. We partially compensate for any such biases by inspecting the ground-based K-band image together with the *HST* /WFPC2 NIR channel.

Each galaxy in our sample of 102 EROs was classified individually by four of the authors (A. Hempel, M. Prieto, I. Trujillo and M. Balcells). Sources for which at least three classifications agree are considered as 'secure'. Besides the *HST* /F814W image, in a few cases we used either the radial profile or the surface brightness isophotes to refine our classification. Initially, we aimed at

[1] http://deep.berkeley.edu

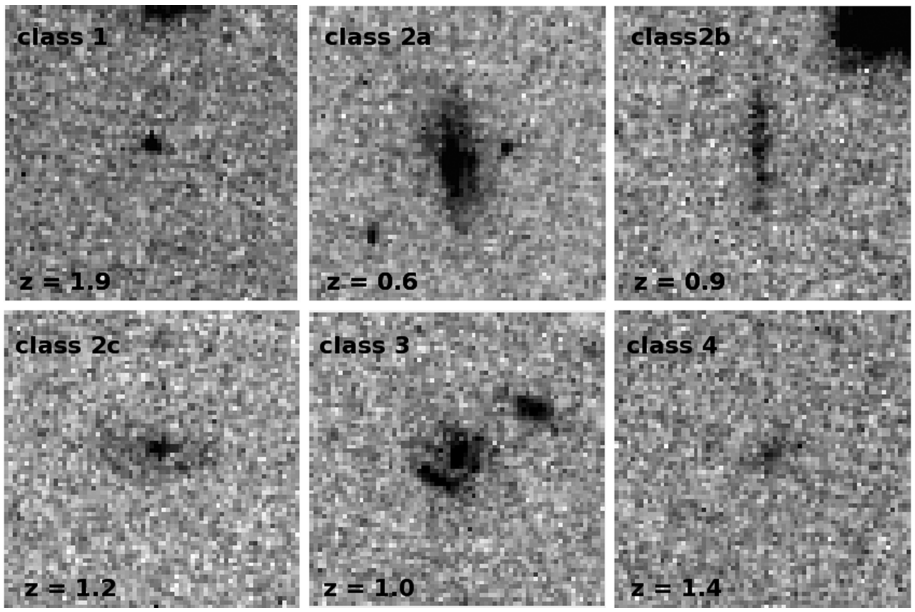

Figure 3. *HST* WFPC2 F814W images of the different morphological classes. The panels are 7.0 arcsec in size, N is up and E left.

classifying three different morphological types: compact for early-type galaxies; extended for disc types and irregular and merging. However, the second class proved to be quite diverse, containing both galaxies with a bulge and a disc component and galaxies which show no clear bulge component. An examples for each class which show a distinct morphology can be seen in Fig. 3.

Finally we differentiate between six classes:

(i) class 1: objects with very compact morphology, like expected for early-type galaxies;
(ii) class 2a: objects with bulge and disc component (early-type discs);
(iii) class 2b: disc galaxies with no clear bulge component, including edge-on discs (late-type discs);
(iv) class 2c: extended objects with bulge and/or disc component, for which no clear classification as either class 2a or class 2b was possible;
(v) class 3: irregular or merger candidates;
(vi) class 4: no clear classification at all.

We complemented the visual classification with a 2D surface-brightness fit of each source in our EROs sample, in order to compare the result of both methods, to determine physical sizes and to explore the mass-size correlation between the different morphological classes.

The structural parameters were estimated with the GALFIT package (Peng et al. 2002), using the *HST* /WFPC2 F814W. GALFIT simultaneously fits several parameters of an analytic light distribution, thereby minimizing χ^2, the residual between the original image and the model. As a result we can describe the global morphology of our objects in terms of structural parameters, like sizes (given as half-light radius or effective radius $r_{\rm eff}$ along semimajor axis $a_{\rm e}$) and Sérsic index n.

All our targets were modelled with a Sérsic profile $[I(r) \propto \exp(-(r/r_{\rm eff})^{1/n})]$. Despite our morphological classification, we keep also the Sérsic index as free parameter, hence not forcing a pure de Vaucouleurs profile ($n = 4$) on 'elliptical' EROs or exponential disc profiles ($n = 1$) on objects with bulge and disc components. All models were convolved with a PSF obtained from unsaturated stars in the image and extremely bright close-by neighbours were masked. The initial values for the parameters to be fitted were derived by SEXTRACTOR. For objects where derived parameters like magnitude, size or position seemed extremely off, the models were tuned by keeping either $I_{\rm mag}$ or the position fixed. Fig. 4 presents examples of the results, using a single Sérsic profile.

Results of the morphological classification are presented in paragraph 5.1.

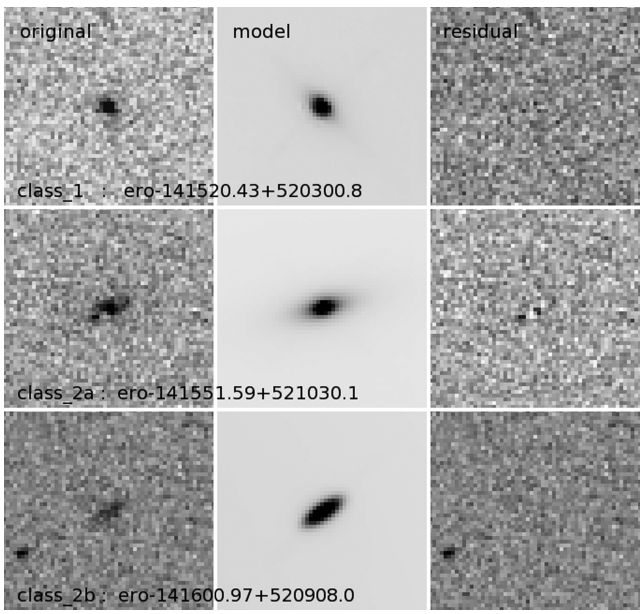

Figure 4. Examples of the *HST* /WFPC2 surface brightness modelling with galfit. For one galaxy of class 1, class 2a and class 2b we modelled a single Sérsic profile (middle column), the panels on the right show the residual image. Each panel is 5.5 arcsec in size.

4 DETERMINING STELLAR MASSES AND AGES

Stellar masses are estimated by fitting the photometric data to synthetic spectra convolved by the filter transmission function, assuming a known photometric redshift. We use magnitudes corrected for aperture effects and scaled to the best-fitting spectral energy distribution, which also provides the value for photometric redshift. For five objects this procedure produces K-band magnitudes fainter than the detection limit and hence were excluded at this point.

EROs with a compact morphology are considered to be old evolved systems, whose stellar population formed in a burst like event over a time span much shorter than their age. As such, population models comprising a single stellar population (SSP) or composite population 'τ-models' with rapidly declining SFR ($\propto \exp(-t/\tau)$) should be adequate. For morphologically extended EROs, for their similarities with galaxy discs, τ-models with more extended values of τ should provide a reasonable approximation to their star formation history. The masses presented here are therefore estimated using τ-models. Clearly, the true SFH of these galaxies may be more complex, and we have fitted each galaxy SED with composite populations comprising a SSP and a τ-model. However, considering the small number of available bands, these models suffer from too much degeneracy.

The model predictions are based on the models from Charlot and Bruzual (Bruzual 2007), and both stellar mass and age for various star formation histories were derived (see Section 4.1). The term 'age' indicates the time between the start of the last episode of star formation (z_f) and the time these galaxies were observed, and therefor represents a 'upper' limit. To simplify, we use 'mass' as synonym for 'stellar mass' throughout the paper.

4.1 Models

Independent of morphology, we have modelled all EROs with the same set of models and parameters, described in Table 1.

The extinction was modelled with the Calzetti extinction law (Calzetti et al. 2000), assuming an average inclination, i.e. orientation effects were not included.

The fitting procedure determines which combination of mass and age produces the best fit to the photometric data.

From all models (624 models for each ERO) we selected the one with the lowest χ^2 as best fit. Fig. 5 shows an example for the χ^2 values obtained for one specific ERO (ero_141715.09+522142.6), one of the EROs with a compact morphology.

The shaded area (upper left plot) identifies the models with $\chi^2 - \chi^2_{\rm best} \equiv \Delta\chi^2 \leq 2.3$, representing a confidence interval of 68.3 per cent assuming two free parameter, stellar mass and age. The majority of models fit the available data poorly, but 10 models result in χ^2 values similar to the best solution (for two pairs of models the χ^2 values can not be separated in this plot). The stellar mass for these models ranges from $0.7 \times M_{\rm best}$ up to $1.8 \times M_{\rm best}$.

Table 1. Model parameter for mass estimates.

Parameter	Range
IMF	Salpeter
Redshift of last SF [a]	$z_f = 3$–8, $\Delta z = 1$
Age limit (Gyr)	0.01 – age$_{\rm universe}$ at z
Exponential decay time (Gyr)	0.05, 0.1, 0.5, 1.0, 4.0, 7.0
Metallicity /$Z_\odot$	0.2, 0.4, 1, 2.5
A_V (Calzetti extinction law)	0.6, 1.0, 2.0, 3.0

[a]Redshift at which the last episode of extended star formation started.

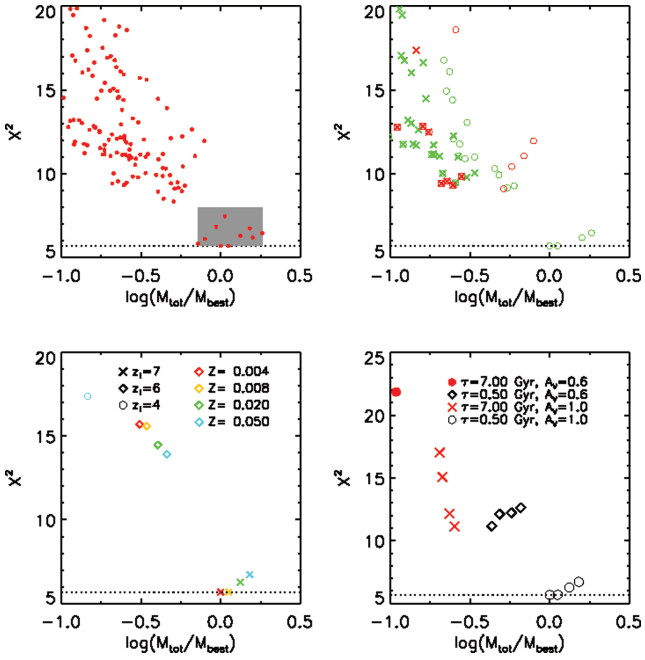

Figure 5. Example for the variation of χ^2 as result of template fitting (ERO: ero_141715.09+522142.6). The dotted line represents the minimal χ^2 value. The masses have been normalized to the mass of the best solution $M_{\rm best}$. Upper left: lower χ^2 values for all possible parameter settings. The shaded region indicates the mass range where $\chi^2_{\rm min} - \chi^2 \leq 2.3$, representing a confidence interval of 68.3 per cent with 2 degrees of freedom (mass and age of the stellar population). Upper right: The symbols represent different formation redshifts: $z_f = 4$ and 8 (cross, open circles). The colours show different values of A_V: red: $A_V = 0.6$, green: $A_V = 1.0$ and blue: $A_V = 2.0$. The metallicity and exponential decay time cover the whole range. Lower left: $A_V = 0.6$, $\tau = 0.5$ Gyr, $z_f = 4$, 6 and 7 (cross, diamond, open circles). Lower right: models with $z_f = 7$, maximal or minimal decay times ($\tau = 0.5$ Gyr: black), $\tau = 7$ Gyr: red), metallicity: not restricted.

In the remaining three panels we kept some of the model parameters fixed, in order to better separate the influence of specific parameters on χ^2. The upper right plot shows the influence of formation redshift (symbols) and dust content (colour), while the other parameters (metallicity and exponential decay time) cover the whole range. For this specific object, models with higher formation redshifts and low extinction show significant better results. Nevertheless, the quality of these models does not improve very much by varying additional parameters like metallicity and exponential decay time. The combination of these parameters might change the stellar mass considerably (as seen in the upper left panel), without improving the quality of already 'good' fits.

In the lower left panel we compare only models with an extinction of $A_V = 0.6$ and $\tau = 0.5$ Gyr. We can see, that for $z_f = 6$, the metallicity improves the fit quality significantly, while the stellar mass increases only slightly. A formation redshift $z_f = 7$ provides better results in general, however, changing the metallicity does not lead to a lower χ^2. In general, the initial metallicity becomes less influential if the object has been formed at earlier times. The lower right panel in this figure shows models with $z_f = 7$, $\tau = 0.5$, 7.0 Gyr and $A_V = 0.6$, 1.0. All models shown by the same symbol and same colour vary only in their initial metallicity. It becomes clear that for longer exponential decay times, the initial metallicity becomes

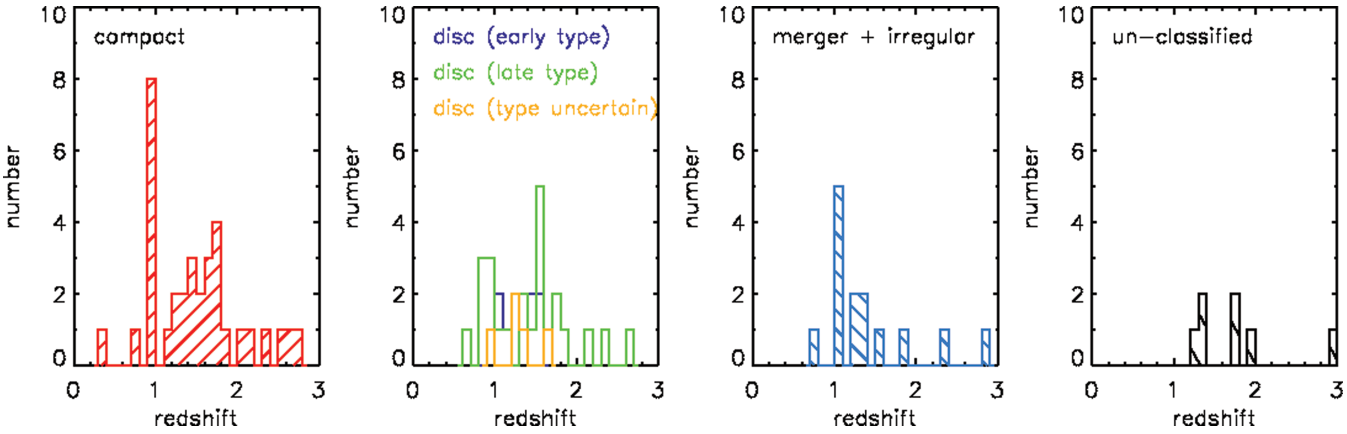

Figure 6. Redshift distribution for all classes. The second panel shows the result for all objects with bulge and disc component, disc-dominated objects and objects which could not be clearly classified as belonging to either of those.

more important. The χ^2 values for $\tau = 0.5$ Gyr and $A_v = 0.6$ and 1.0 vary noticeable less than for $\tau = 7.0$ Gyr.

This plot clearly illustrates that all the parameters influence each other in non-linear way, e.g. the effect of one parameter on χ^2 does not have to be constant, if one of the remaining parameters changes.

At the moment we have not calculated the error in age and mass, however, the plot shows that the later can vary by a factor of 2.5 with almost constant χ^2, depending on the specific SED template. At the same time, the age for this object will vary by less than 30 per cent. Such uncertainties in stellar mass agree well with the results of Elsner, Feulner & Hopp (2008), who estimated that errors in redshift, M/L_K ratio, photometry and errors attributed to template fitting can add up to a mean uncertainty of about $\sigma_{\log M} = 0.33$ dex. For an extensive study of stellar mass estimators, their limitations and uncertainties see Longhetti & Saracco (2009).

5 RESULTS

In this section we present our results regarding morphologies, stellar masses, ages and their evolution. Our catalogue is presented in tabular form in the Appendix in Tables A1 and A2, where we list both photometric, morphological, structural and stellar population parameters. Fig. 6 shows the redshift distribution for each morphological class (see Section 3). The sample of compact objects (class 1, upper left panel in Figs 12 and 13) and EROs with bulge and/or disc component (class 2a,b,c, upper right panels in Figs 12 and 13) show the clearest redshift distributions, with a peak between redshift 1 and 2. The large number of compact objects with redshifts of $0.9 \leq z_{\rm phot} \leq 1.0$ can not be explained by pure low number statistics, hence we looked at the spatial distribution of compact EROs in this region (Fig. 7). Four of the compact objects lie within a field of 1.1 arcmin radius (0.5 Mpc at $z = 0.95$). The large number of such EROs in a very narrow redshift bin hints at an overdensity of compact objects, as we find only a total of eight such galaxies in the whole 155 arcmin^2 field. The resulting surface density is 20 times higher than the average value. However, the four EROs lie in an interval $\Delta z_{\rm phot} = z_{\rm max} - z_{\rm min} = 0.07$ which, given our typical $z_{\rm phot}$ errors, is consistent with zero. In order to proof the physical association of these EROs, spectroscopic redshifts are required.

In Fig. 8 we show a summary of the photometric properties [colour versus apparent magnitude (K_s), absolute magnitude (M_K)

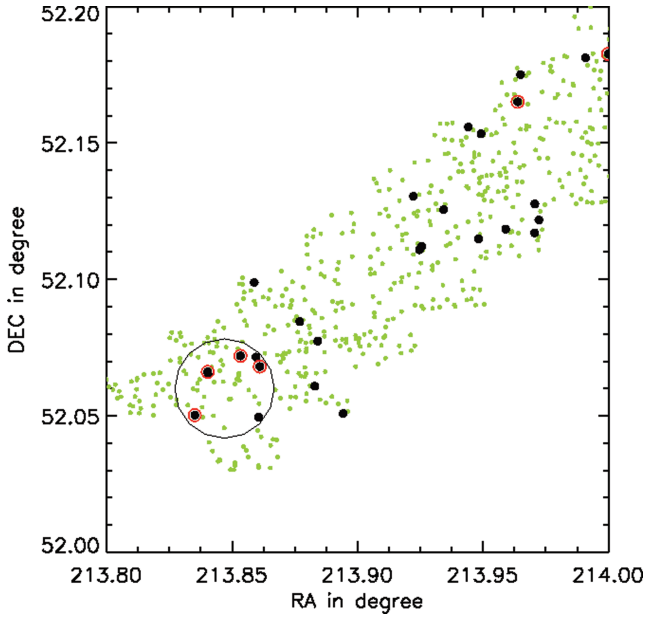

Figure 7. Spatial distribution of EROs in a section of Groth Strip. The black symbols show all EROs in this section of the field, red circles mark compact objects (class 1) with redshifts of $0.9 \leq z_{\rm phot} \leq 1.0$. The black circle with a radius of 1.1 arcmin, corresponds to 0.5 Mpc at redshift 0.95.

and redshift] of our EROs sample. We detect EROs from the detection limit of our survey, $K_s \sim 21$, up to $K_s \approx 18$. In Fig. 8, left-hand panel, the distribution in colour-apparent magnitude has an apparent triangular shape, such that the reddest EROs are only found at intermediate apparent magnitudes. On the faint side of this distribution, this is due to an observational bias given by the detection limit in $F814W$. On the bright side, the trend is real. It originates from the fact that the reddest EROs are among the most intrinsically luminous of the sample, as portrayed in the central panel of Fig. 8, which shows observed colour against K-band absolute magnitude. We detect a mild colour–absolute magnitude relation, but no significant trend of colour with redshift (right-hand panel of Fig. 8).

All morphological classes are found at all magnitudes and colours, nevertheless, most of the faint objects with irregular of merger characteristics have bluer colours than their brighter

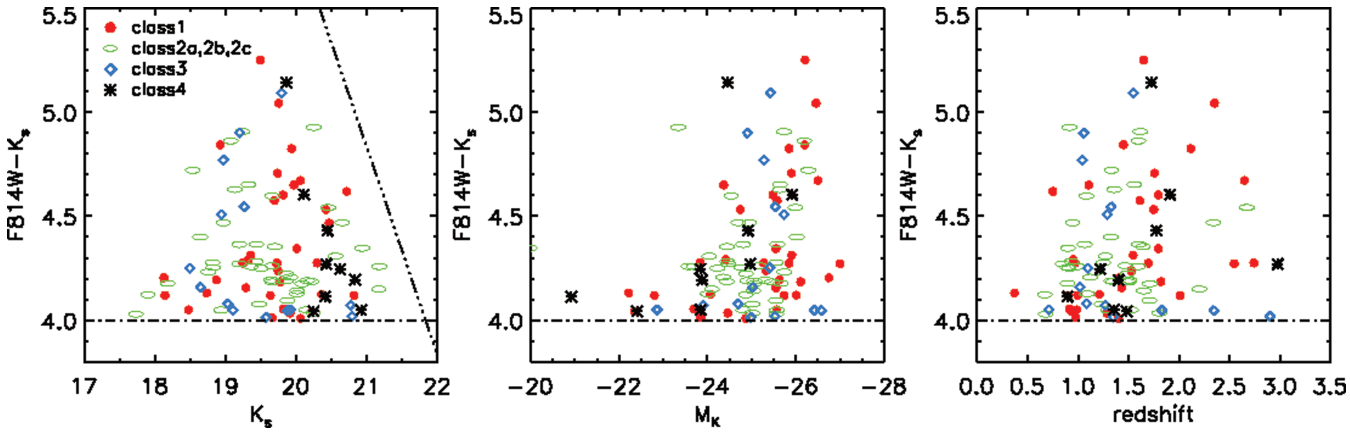

Figure 8. Photometric properties of the complete EROs sample: dependency of $F814W - K_s$ colour on K_s, M_K and redshift. The same symbols and colours are used in all three panels, the sloped line indicates the colour limit assuming a detection limit of $F814W_{lim} = 25.8$.

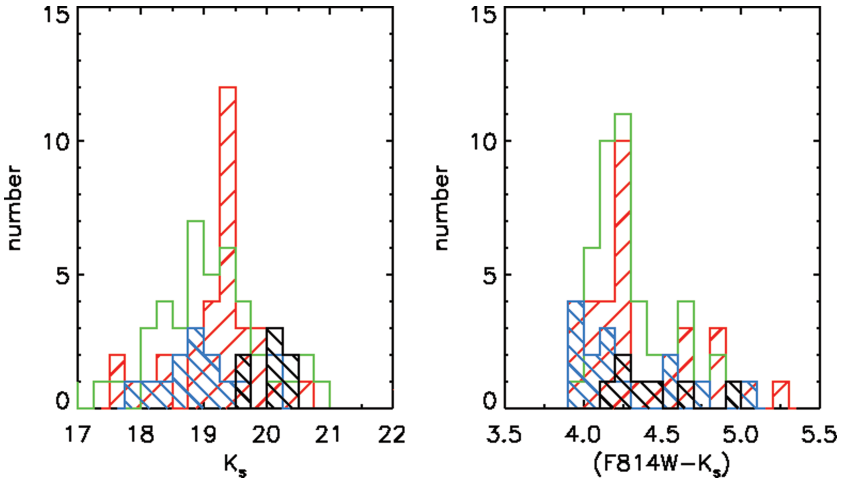

Figure 9. K_s-magnitude distribution (left-hand panel) and F814W$-K_s$ colour distribution (right-hand panel) for our EROs sample, The colours are based on the magnitudes derived from the best-fitting SED, and not aperture magnitudes. The red histograms represent EROs of class 1, green indicates objects of class 2 a,b and c, i.e. EROs with discs. Irregular galaxies or merging candidates and not classified objects are shown in blue and black.

counterparts. Brighter EROs ($K_s \leq 19.5$) are slightly dominated by disc-like morphologies and EROs with an undetermined morphology are found at the fainter magnitudes (see also Fig. 9). Based on our data set, we see no clear distinction of the photometric properties between the morphological classes.

5.1 Morphology

From the visual classification of our sample we find that 34 ± 6 per cent of our EROs have a compact morphology and 43 ± 6 per cent have a disc component. Irregular galaxies and merger candidates contribute 14 ± 4 per cent, while 9 ± 3 per cent are not classifiable due to low image quality. The uncertainties are quoted solely on the basis of the statistical error of the number of EROs in this morphological class.

Our result agrees well with Gilbank et al. (2003), who also find an almost equal fraction of spheroidal/compact EROs and disc-like objects among a sample of 224 EROs ($K < 20, I_{814} - K) \geq 4.0$), 30 and 35 per cent, respectively. 15 per cent of their EROs show a disturbed/irregular morphology. Nevertheless, this result is in contradiction to Yan & Thompson (2003) and Moustakas et al. (2004). The former performed a visual classification of 115 EROs ($F814W - K_s \geq 4$, 5σ median limiting K_s magnitude of $\approx$18.7) into four broad categories: spheroids or pure bulge galaxies, bulge-dominated galaxies, disc-like systems with some evidence of a bulge and discs which show no obvious bulge component. Yan and Thompson use the same data set (MDS) as Gilbank et al. and find that approximately 66 per cent of their EROs are discs or disc dominated and only 34 per cent have morphologies consistent with bulges or are bulge dominated. These numbers refer to a total of 101 EROs (out of 115) for which the visual classification is either bulge, bulge dominated, discs or disc dominated. However, our results agree in regard to a large fraction of edge-on spirals, 57 ± 11 per cent of EROs with discs show such an orientation, compared to 40 per cent in the Yan et al. sample. Moustakas et al. find a combination of 36 per cent early-type galaxies, 55 per cent late-type and 5 per cent irregulars.

The most secure classifications of our sample (i.e. at least three out of four classifiers agree) have been obtained for the objects in class 1 (34 of 35), class 2a (13 of 13) and class 2b (25 of 25). The classification for the members of class 2c and class 4 is the least reliable, almost no object in either class (5/5 and 8/9 for class 2c and class 4, respectively) shows an easy to distinguish or unique morphology. For class 3, consisting of irregular and merger candidates, the classification is secure in about 50 per cent (8 of 14) of the sample.

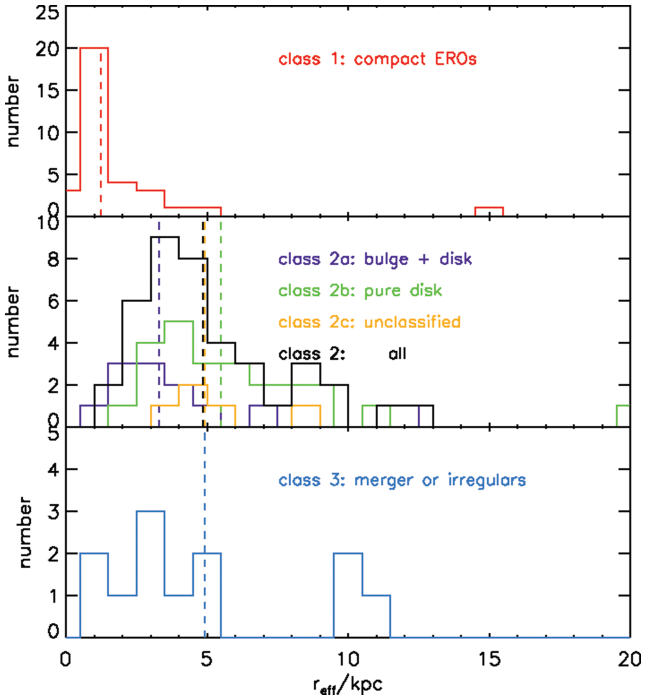

Figure 10. Distribution of effective radius (for different morphological classes). The black solid line in the central panel shows the result for the total of class 2.

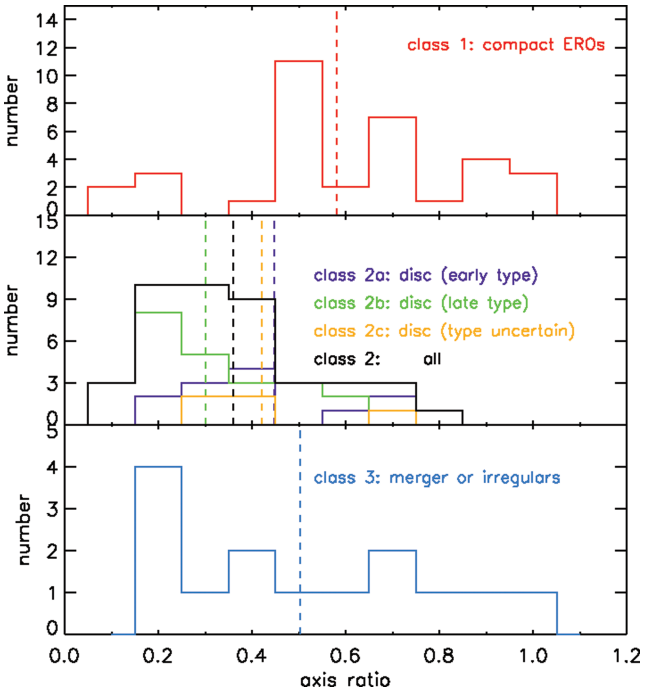

Figure 11. Comparison of the axis ratios (derived with galfit), for all morphological classes. Colours are assigned to morphological class as in Fig. 10.

5.2 Structural parameters

In Table A1. we list effective radii, Sérsic index, axis ratios and model magnitudes, with their errors, for all of the EROs as produced by galfit (if not stated otherwise, the effective radii are not circularized), Fig. 10 shows the results of the structural analysis for the different morphological classes. For six objects with a compact or undetermined morphology (5+1 objects of class 1 and class 4, respectively), the effective radii are extremely small, $\lesssim$0.1 kpc. The visual inspection of the original images revealed, that these EROs are barely resolved and although the overall quality of the fit is comparable to the other targets, all parameters show large errors and are very likely faint stars instead of galaxies (these objects have been marked in Table A1). On this basis we excluded these objects from our analysis.

The EROs with compact morphology show the smallest median effective radii (1.19 ± 0.14 kpc), followed by EROs of mixed morphology (bulge+disc) and disc dominated, 3.31 ± 0.53 kpc and 5.38 ± 0.50 kpc, respectively. Objects which could belong to either of the last two classes (objects with class 2c morphology) have median sizes of 4.91 ± 0.14 kpc. Sources which appear irregular or might be part of an ongoing merger and hence show a disturbed morphology have median sizes of about 4.92 ± 1.06 kpc. The median size of objects with no discernible morphology (class 4) is 2.59 ± 0.69 kpc.

The median Sérsic index for our compact EROs (class 1), $n = 2.30 \pm 0.34$, is within the errors, in the range for quiescent galaxies, $n \geq 2.5$, used by Trujillo et al. (2007), based on the comparison with local galaxies. EROs which appear to be pure discs or at least disc dominated are best fitted with a Sérsic index of $n = 1.03 \pm 0.24$, compared to a Sérsic index of 1 for exponential profiles. Objects with bulge and disc components have a median Sérsic index of $n = 3.24 \pm 0.55$. This implies that the light distribution seems to be dominated by the bulge component, similar to the compact objects in class 1. The result for irregulars or merger candidates ($n = 1.54 \pm 0.40$) lies between compact EROs and disc dominated objects, as we have seen for the effective radius. A median Sérsic index of $n = 5.06 \pm 1.61$ would imply a very steep surface brightness profile for objects with an unclassified morphology, however, the images have either a low quality and/or the targets are almost unresolved.

In our visual classification we consider 'edge-on' disc dominated as separate morphological class (class 2b) and we would expect that these objects show smaller axis ratios (semiminor axis/semimajor axis) than the other morphological types. The plot in Fig. 11 confirms this expectation, showing an increasing axial ratio from an apparent 'edge-on' morphology, to 'disc+bulge' morphologies and the more compact elliptical EROs (0.3 ± 0.03, 0.45 ± 0.06 and 0.62 ± 0.04, respectively).

Using the masses determined in Section 4, we show in Fig. 17 the stellar mass–size relation for EROs. The dot–dashed line shows the relations for early-type galaxies ($n \geq 2.5$) and the dashed line for late-type galaxies ($n < 2.5$), based on the analysis of SDSS galaxies by Shen et al. (2003). This figure shows that compact galaxies deviate more clearly from the local relation than the other morphological types, supporting the strong evolution of the stellar mass–size relation, as described by Trujillo et al. (2007) for the most massive galaxies.

5.3 Stellar masses

We now present stellar masses for 97 EROs in our sample, computed as outlined in Section 4. The output of the mass code, namely stellar mass and population age, are shown against redshift in Figs 12 and 13, respectively (see also Table A2). The vertical error bar in the top-left panel of Fig. 12 indicates the typical uncertainty of 0.3 dex. In Fig. 13, where ages are shown against redshift, lines correspond to formation redshifts as detailed in the legend. The median and rms of the total stellar mass of each morphological class are given in Table 2, and displayed in Fig. 14. Stellar masses for our ERO

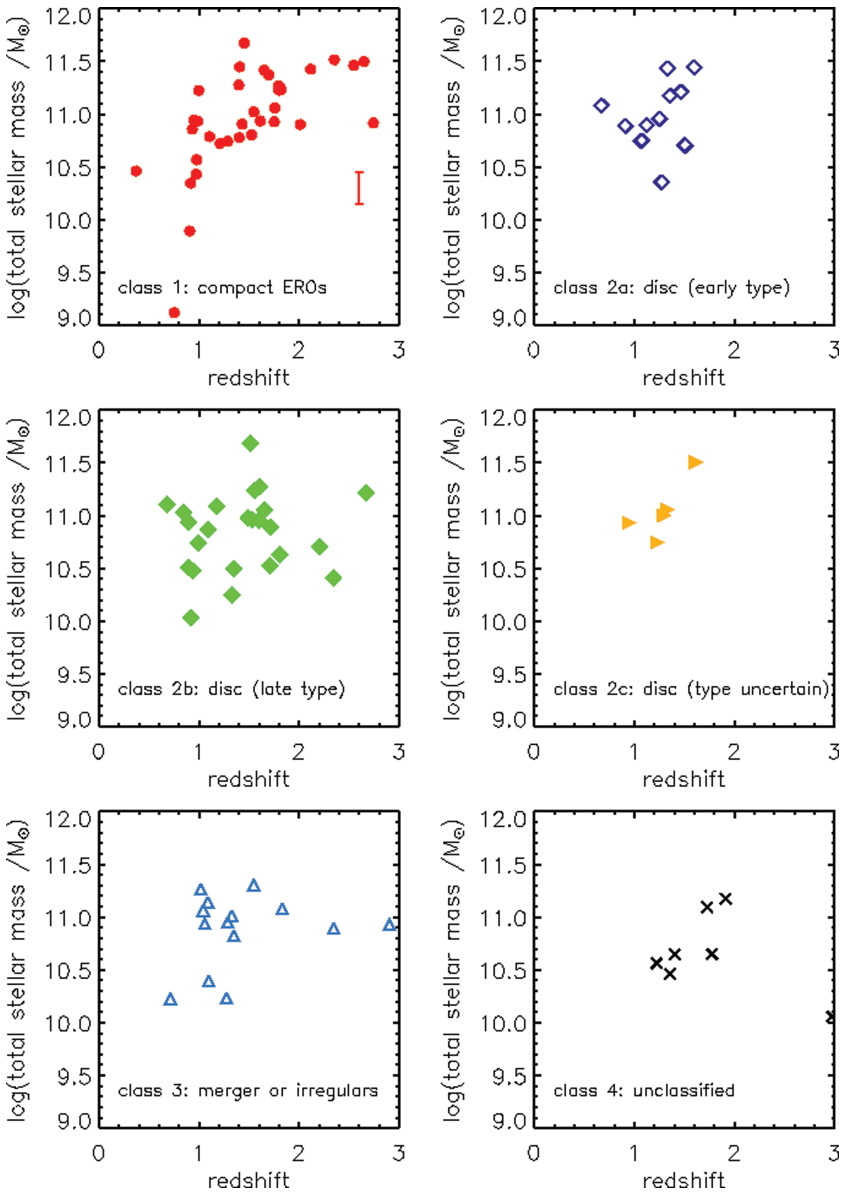

Figure 12. Total (stellar) masses for all morphological classes. The error bar in the upper left panel indicates the uncertainties in the mass estimates based on the SED fitting ($M_{\rm max}/M_{\rm min} = 2$).

sample range from $\log(M/{\rm M}_\odot) = 10.0$ to $\log(M/{\rm M}_\odot) = 11.8$. Median stellar masses lie between $\log(M/{\rm M}_\odot) = 10.7$ and 11.0. The median masses change little from one morphological class to another. Such independence of stellar mass with morphological class is the main result of this paper. This result was not expected. The common understanding that the most massive galaxies are ellipticals led us to expect EROs with disc or (major) merger morphologies to have significantly lower masses than EROs with compact morphologies. One third of the EROs with a disc dominated morphology (24 EROs in class2b) have masses above $10^{11}{\rm M}_\odot$ suggests a mechanism to build up massive galaxies that does not involve dissipationless mergers. Such galaxies may have grown through cold accretion (Dekel et al. 2009); alternatively, massive disc-shaped EROs, which must contain vast amounts of dust, are also candidates for remnants of very gas rich major mergers (Hopkins et al. 2009). That EROs include disc-shaped objects with a range of bulge prominence may indicate that the build-up of bulge components in disc galaxies between redshifts 2 and 1 (e.g. Dekel, Sari & Ceverino 2009) includes important dusty phases.

Due to the large scattering in mass between the members of each class and the low numbers, no significant difference in median stellar mass is evident, including the EROs belonging to class 4, whose mean stellar mass [$\log({\rm M/M}_\odot) = 10.7$] differs by approx. 1σ from the other morphological classes (see Fig. 14).

Below we discuss each morphological class in more detail.

(i) *Class 1: compact EROs*. The compact morphology of these objects is rather distinct and closely resembles those of an elliptical galaxy with a dominant old stellar population and no or very low ongoing star formation. For most EROs (21 of 34) in this sample the decay times are 100 Myr and less, i.e. the period of star formation is extremely short and on first look resembles a single burst. However,

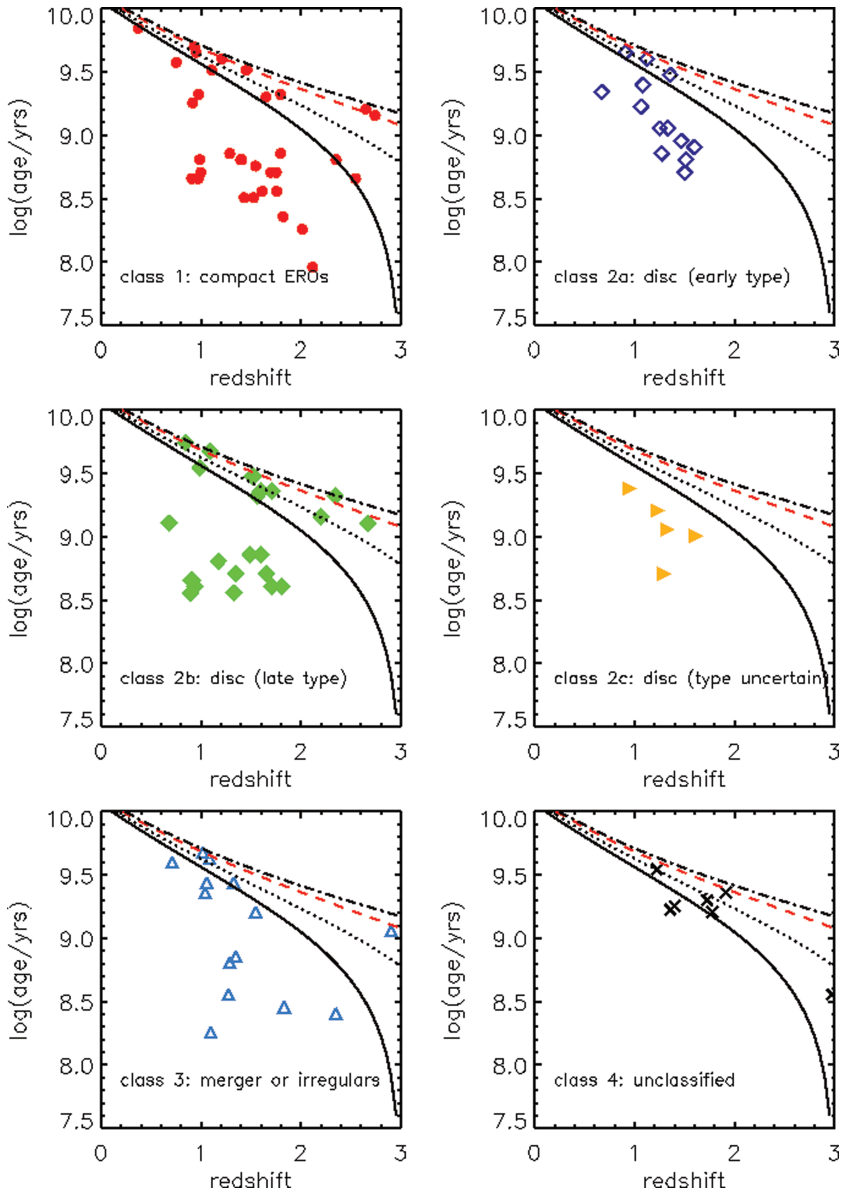

Figure 13. Stellar ages based on an exponential declining star formation. The lines correspond to the maximal possible age for a galaxy formed at $z_f = 8$, 6, 4, 3, if observed at the given redshift (from top to bottom, red line corresponds to $z_f = 6$).

Table 2. Median of total stellar mass, size (a_e) and Sérsic index (n) for each morphological class. The results for r_{eff}) and Sérsic index consider only the EROs for which also masses are available. We have excluded objects which diver more than 3 standard deviations from the median value.

Morphological class	log($M_\star$)	σlog($M_\star$)	size (a_e) (kpc)	σa_e (kpc)	n	σn
Class 1 : compact	10.99	0.07	1.22	0.14	2.30	0.34
Class 2a : disc + bulge	10.95	0.09	3.31	0.53	3.24	0.55
Class 2b : pure (edge-on) disc	10.93	0.08	5.50	0.51	1.03	0.24
Class 2c : disc + bulge (unclassified)	10.93	0.07	4.91	0.14	1.72	0.40
Class 3 : irregular or merger	10.98	0.07	4.92	1.06	1.54	0.40
Class 4 : unclassified	10.69	0.13	2.59	0.69	3.89	1.56
All:	10.66	0.04	3.48	0.29	2.07	0.20

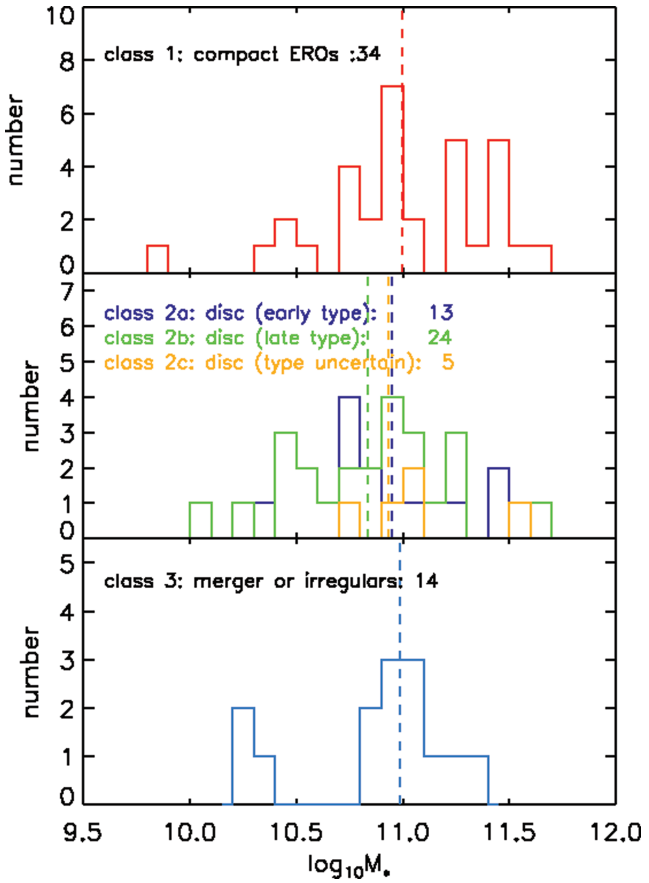

Figure 14. Distribution of total stellar mass for distinct morphologies. The vertical lines show the median of each distribution (see Table 2).

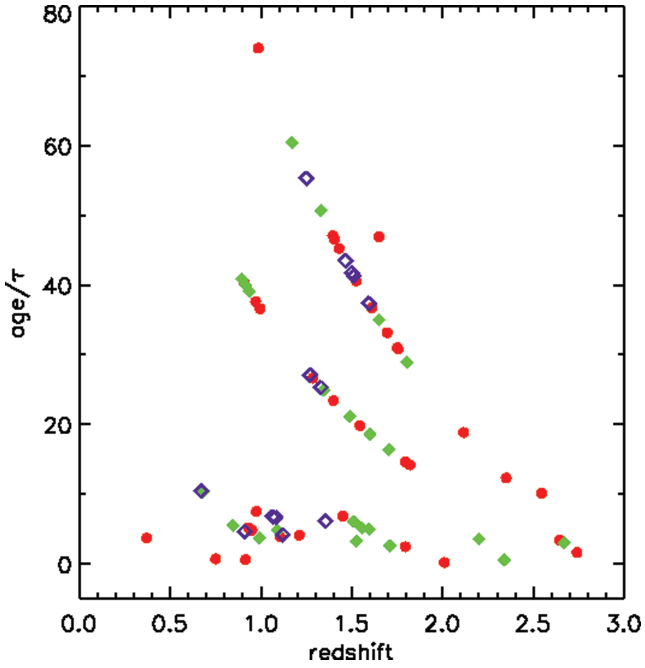

Figure 15. Ratio between population age at the time of observation and the exponential decay time τ against redshift, for EROs with compact morphology (red), bulge+disc (purple) and disc dominated (green).

Fig. 15 illustrates that for some objects the ratio between $t(z_f) - t(z)$ and τ is rather small, indicating that these EROs might still form a certain amount of stellar mass. Using a threshold of age/$\tau = 6$ (Fontana et al. 2009) to separate active and quiescent galaxies, 67 ± 14 per cent (23/34) of our compact galaxies qualify as quiescent. The fraction of quiescent galaxies among the 'bulge+disc' galaxies is 84 ± 25 per cent (11/13), and drops to 58 ± 15 per cent (14/24) for disc dominated galaxies. Combining the galaxies which are either pure bulges (class 1) or show bulge+disc structure (class 2a), we find that approximately 72 per cent (34/47) of this subsample would qualify as quiescent galaxies.

Nevertheless, we find that more than 50 per cent of the entire compact ERO sample have ages of less than 1 Gyr. The youngest object in this class has an apparent age of 0.1 Gyr.

The deficiency of low-mass objects ($M < 5 \times 10^{10}\,M_\odot$) at higher redshifts is result of the limited depth of our survey. This impression is largely caused by two $z \sim 1$ objects with masses $\log(M/M_\odot) < 10$. We have tested the detectability of these two low-mass objects at higher redshifts by simulating their appearance as a function of z, assuming passive evolution (Fig. 16). The simulations show that the lack of low-mass objects at higher redshift is the result of the limited depth of our survey.

(ii) *Class 2a, 2b and 2c: EROs with disc component*. In this class we find no objects with masses below $\log(M/M_\odot) < 10$. Contrary to the compact class, objects with disc components and with masses between $10.2 < \log(M/M_\odot) < 11.5$ are found in the whole redshift range, up to redshift 2.5. This behaviour is clearly visible in panels assigned to class 2 objects in Fig. 12. The mass distributions of the three subclasses differ due to the limited redshift intervals where objects of each class are found, the mean stellar of all morphological types (with disc component) agree well within their accuracy (see Table 2).

Similar to compact EROs, we find a significant number of objects with stellar populations of more than 1 Gyr of age, both among EROs with and without bulge component. However, no object seems to be younger than 0.3 Gyr, although we would expect these to have lower ages than the compact EROs. For approximately 2/3 of this population, the last star formation event started not later that $z_f = 3$ (see also Fig. 13).

(iii) *Class 3: irregular/merging EROs*. The majority of objects in this class have masses of approximately $10^{11}\,M_\odot$, similar to the masses of compact objects or disc-like systems. For none of these objects the last episode of star formation started later than redshift 4, suggesting that population ages of less than 1 Gyr are the result of continuous star formation.

(iv) *Class 4: unclassified*. The median stellar mass of this class is slightly lower, $4.6 \times 10^{10}\,M_\odot$. Like the irregular or merging EROs, the members of this class started forming their stellar mass very early, at redshift 4 and higher. With one notable exception, the ERO at redshift 2.98 (ero_141755.44+522928.5), the stellar population in this group is older than 1 Gyr.

Considering that the mass estimates can vary by factors of 2, we find no dependency of average total mass on the morphological type of our ERO sample. The stellar mass–size relation (Fig. 17) shows a clear dependence on morphological type, with compact galaxies (class 1) having significant smaller sizes than EROs with different morphologies.

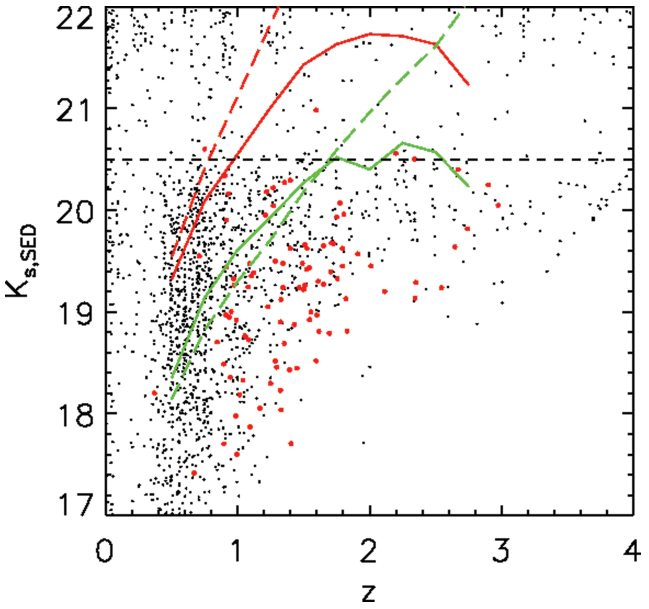

Figure 16. K_s distribution for galaxies in Groth (black dots) and selected EROs (red dots). The lines are K_s-band magnitudes derived from evolving the spectral energy distribution of two low mass EROs and the model used to fit these SEDs. The two objects have redshifts of 0.75 (red) and 0.905 (green), and total stellar masses of 0.13×10^{10} and $0.78 \times 10^{10}\,M_\odot$ respectively. The solid lines represent a SSP model, the dashed line a model with extended star formation. The horizontal line represents a measure of our limiting K-band magnitude.

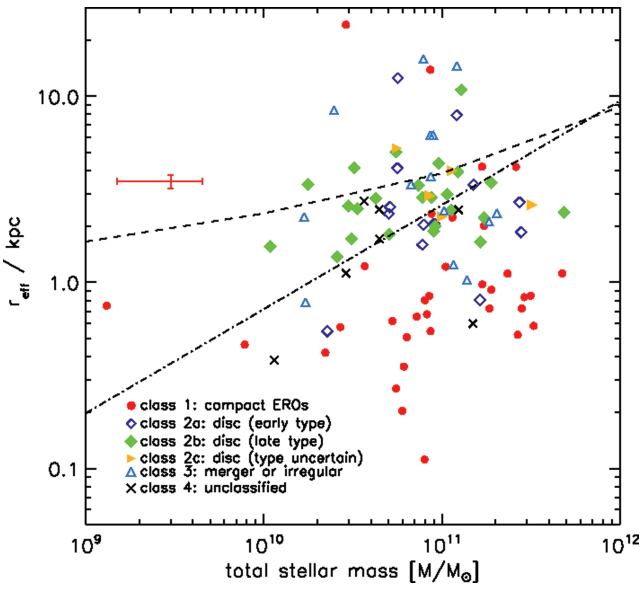

Figure 17. The (stellar) mass size distribution for all morphological classes. The effective radii are circularized, $r_{\rm eff} = a_{\rm e}\sqrt{(1-\epsilon)}$, with ϵ being the ellipticity of the object (1-axial ratio). The dot–dashed line shows the local mass size of early-type galaxies ($n \geq 2.5$) and the dashed line for late-type galaxies ($n < 2.5$) the SDSS (Shen et al. 2003). The stellar mass has been evaluated using a Salpeter IMF. The error bars represent a possible uncertainty in mass by a factor of 2, and the standard deviation for $r_{\rm eff}$ (see Table 2).

SUMMARY

In this paper we have presented a sample of 102 extremely red galaxies with $F814W - K_s \geq 4$ found within the GOYA Survey. The EROs morphology was visually classified. We found an almost equal fraction of compact objects (37 per cent) and objects with a disc component (40 per cent). Among the later we find a substantial fraction of edge-on spirals, 58 per cent of all class 2 objects, which is extremely good agreement with the results of Gilbank et al. (2003) and Yan & Thompson (2003). However, there is a discrepancy between the fraction of edge on spirals in respect to the total ERO sample of Yan & Thompson (2003).

Our visual classification agrees well with the results of 2D surface brightness fitting (galfit), showing that galaxies which appear compact have both smaller effective radii and larger Sérsic indices than galaxies with bulge+disc components (larger $r_{\rm eff}$ but also larger Sérsic index). Pure 'disc galaxies' have both the largest effective radii and the smallest Sérsic index, while the irregular galaxies or merger candidates seem to represent an intermediate state.

Photometric masses were derived by fitting Charlot & Bruzual (Bruzual 2007) τ-population models to the SED of the galaxies. Derived stellar masses for our ERO sample range from $\log(M/M_\odot) = 10$ to $\log(M/M_\odot) < 11.6$. Our median stellar mass is $\log(M/M_\odot) \approx 11.0$. Most notably, the median stellar mass is independent of morphology, arguing against the notion that massive galaxies are spheroids. We note that some of the EROs at high redshift ($z > 2$), have ages close to the age of the Universe at the redshifts they are observed, which in case of compact objects poses a challenge to the current models of galaxy formation, in which evolved galaxies form at later times through the merger of low mass objects. However, the young objects in class 1 agree well with merger scenarios (see also Ricciardelli et al. 2010).

We do not observe a strong evolution within $1 < z < 2$ for $10^{11}\,M_\odot$ mass objects, neither among the compact class nor for EROs with a star forming component. Similar results have been found by Conselice et al. (2008) for massive EROs with $M_\star > 10^{11}\,M_\odot$ detected in the DEEP2/Palomar fields. The EROs within their $K < 19.7$ selection have the same upper range of masses at $z \sim 0.8$–2.0, therefore indicating little mass growth for this population at this K-band limit. Also we detect a substantial fraction of EROs with total stellar masses below $10^{11}\,M_\odot$ while Conselice et al. (2008) state that almost all of their EROs at $K < 19.7$ have masses above this value.

Looking at the mass–size relations we find that our sample of compact galaxies deviates strongly (circa factors of 4–5) from the local relation, while the galaxies in the remaining morphological classes lie closer to the local mass–size relation for late-type galaxies, which is in agreement to previous studies like Trujillo et al. (2007).

ACKNOWLEDGMENTS

This work was supported by the Consolider-Ingenio 2010 Programme grant CSD2006-00070: First Science with the GTC and by grants AYA2006-12955, AYA2009-11137 and AYA2010-21322-CO3-02 from the Spanish Ministry of Science and Innovation.

Facilities: *HST* (WFPC2); ING: William Herschel Telescope (INGRID); ING: Isaac Newton Telescope (WFC).

REFERENCES

Abraham R. G., van den Bergh S., Glazebrook K., Ellis R. S., Santiago B. X., Surma P., Griffiths R. E., 1996, ApJS, 107, 1

Afonso J., Mobasher B., Chan B., Cram L., 2001, ApJ, 559, L101

Alexander D. M., Vignali C., Bauer F. E., Brandt W. N., Hornschemeier A. E., Garmire G. P., Schneider D. P., 2002, AJ, 123, 1149
Balcells M., Cristobal-Hornillos D., Prieto M., Guzman R., Gallego J., Serrano A., Cardiel N., Pello R., 2002, Newsletter Isaac Newton Group Telesc., 6, 11
Bolzonella M., Miralles J.-M., Pelló R., 2000, A&A, 363, 476
Brusa M. et al., 2005, A&A, 432, 69
Bruzual A. G., 2007, in Vazdekis A., Peletier R. F., eds, Proc. IAU Symposium 241, On TP-AGB Stars and the Mass of Galaxies, Cambridge Univ. Press, Cambridge p. 125
Bruzual G., Charlot S., 2003, MNRAS, 344, 1000
Calzetti D., Armus L., Bohlin R. C., Kinney A. L., Koornneef J., Storchi-Bergmann T., 2000, ApJ, 533, 682
Cappellari M. et al., 2009, ApJ, 704, L34
Cenarro A. J., Trujillo I., 2009, ApJ, 696, L43
Cimatti A. et al., 2002, A&A, 391, L1
Conselice C. J., 2006, ApJ, 638, 686
Conselice C. J., Bundy K., U V., Eisenhardt P., Lotz J., Newman J., 2008, MNRAS, 383, 1366
Cristóbal-Hornillos D., Balcells M., Prieto M., Guzmán R., Gallego J., Cardiel N., Serrano Á., Pelló R., 2003, ApJ, 595, 71
Daddi E. et al., 2005, ApJ, 631, L13
De Lucia G., Springel V., White S. D. M., Croton D., Kauffmann G., 2006, MNRAS, 366, 499
Dekel A. et al., 2009, Nat, 457, 451
Dekel A., Sari R., Ceverino D., 2009, ApJ, 703, 785
Desai V. et al., 2007, ApJ, 660, 1151
de Vaucouleurs G., 1948, Ann. Astrophys., 11, 247
Domínguez-Palmero L., Balcells M., Erwin P., Prieto M., Cristóbal-Hornillos D., Eliche-Moral M. C., Guzmán R., 2008, A&A, 488, 1167
Dressler A., Lynden Bell D., Burstein D., Davies R. L., Faber S. M., Terlevich R., Wegner G., 1987, ApJ, 313, 42
Eliche-Moral M. C., Balcells M., Prieto M., García-Dabó C. E., Erwin P., Cristóbal-Hornillos D., 2006, ApJ, 639, 644
Eliche-Moral M. C. et al., 2010, A&A, 519, A55+
Ellis R. S., Abraham R. G., Dickinson M., 2001, ApJ, 551, 111
Elsner F., Feulner G., Hopp U., 2008, A&A, 477, 503
Elston R., Rieke G. H., Rieke M. J., 1988, ApJ, 331, L77
Elston R., Rieke M. J., Rieke G. H., 1989, ApJ, 341, 80
Fontana A. et al., 2004, A&A, 424, 23
Fontana A. et al., 2009, A&A, 501, 15
Fu H., Stockton A., Liu M., 2005, ApJ, 632, 831
Gilbank D. G., Smail I., Ivison R. J., Packham C., 2003, MNRAS, 346, 1125
Glazebrook K. et al., 2004, Nat, 430, 181
González-Pérez V., Baugh C. M., Lacey C. G., Almeida C., 2009, MNRAS, 398, 497
Groth E. J., Kristian J. A., Lynds R., O'Neil E. J., Jr, Balsano R., Rhodes J., 1994, BAAS, 26, 1403
Hayashi M., Shimasaku K., Motohara K., Yoshida M., Okamura S., Kashikawa N., 2007, ApJ, 660, 72
Hopkins P. F. et al., 2009, MNRAS, 397, 802
Hu E. M., Ridgway S. E., 1994, AJ, 107, 1303
Huertas-Company M. et al., 2008, A&A, 478, 971
Im M. et al., 2002, ApJ, 571, 136
Kassin S. A. et al., 2007, ApJ, 660, L35
Kauffmann G., White S. D. M., Guiderdoni B., 1993, MNRAS, 264, 201
Kitzbichler M. G., White S. D. M., 2006, MNRAS, 366, 858
La Barbera F., Busarello G., Merluzzi P., de la Rosa I. G., Coppola G., Haines C. P., 2008, ApJ, 689, 913
Labbé I. et al., 2005, ApJ, 624, L81
Longhetti M., Saracco P., 2009, MNRAS, 394, 774
López-Sanjuan C. et al., 2009, ApJ, 694, 643
Maraston C., 2005, MNRAS, 362, 799
Moustakas L. A. et al., 2004, ApJ, 600, L131
Papovich C., 2006, New Astron. Rev., 50, 134
Peng C. Y., Ho L. C., Impey C. D., Rix H., 2002, AJ, 124, 266
Pozzetti L., Bruzual A. G., Zamorani G., 1996, MNRAS, 281, 953
Prieto M., Balcells M., Domínguez-Palmero L., Cristóbal-Hornillos D., Erwin P., Eliche-Moral C., Abreu D., 2005, Revista Mexicana Astron. Astrofis. Conf. Ser., 24, 270
Ratnatunga K. U., Griffiths R. E., Ostrander E. J., 1999, AJ, 118, 86
Reda F. M., Forbes D. A., Hau G. K. T., 2005, MNRAS, 360, 693
Ricciardelli E., Trujillo I., Buitrago F., Conselice C. J., 2010, MNRAS, 406, 230
Roche N. D., Almaini O., Dunlop J., Ivison R. J., Willott C. J., 2002, MNRAS, 337, 1282
Roche N. D., Dunlop J., Almaini O., 2003, MNRAS, 346, 803
Sarajedini V. L. et al., 2006, ApJS, 166, 69
Shen S., Mo H. J., White S. D. M., Blanton M. R., Kauffmann G., Voges W., Brinkmann J., Csabai I., 2003, MNRAS, 343, 978
Simard L. et al., 2002, ApJS, 142, 1
Somerville R. S., Primack J. R., Faber S. M., 2001, MNRAS, 320, 504
Somerville R. S. et al., 2004, ApJ, 600, L135
Stockton A., McGrath E., Canalizo G., 2006, ApJ, 650, 706
Tinsley B. M., Gunn J. E., 1976, ApJ, 203, 52
Treu T. et al., 2005, ApJ, 633, 174
Trujillo I. et al., 2006, MNRAS, 373, L36
Trujillo I., Conselice C. J., Bundy K., Cooper M. C., Eisenhardt P., Ellis R. S., 2007, MNRAS, 382, 109
Tully R. B., Fisher J. R., 1977, A&A, 54, 661
Vaduvescu O., McCall M. L., 2008, A&A, 487, 147
Weiner B. J. et al., 2005, ApJ, 620, 595
White S. D. M., Rees M. J., 1978, MNRAS, 183, 341
Yan L., Thompson D., 2003, ApJ, 586, 765
Yan H. et al., 2004, ApJ, 616, 63

APPENDIX A: TABLE A1

Summary of photometric, morphological and structural parameters [(1) target name, (2) photometric redshift, (3) visual classification, (4) security of the vote, (5) aperture magnitude F814W, (6) aperture magnitude – K_s, (7) colour, (8) size – a_e (half-light radius along semimajor axis), (9) Sérsic index, (10) axial ratio (b/a), (11) F814W magnitude from galfit, (12) reduced χ^2 by galfit]. Objects marked with * fulfil also the colour criteria for DRGs: $J - K > 2.3$. The small photometric errors are SEXTRACTOR errors only. Objects marked with # show extremely low effective radii ($r_{\rm eff} \leq 0.01$ kpc) and were excluded from our final target list.

Table A1. Summary of photometric, morphological and structural parameters. For an explanation of the columns please see the text in this section.

Name	z_{phot}	Class	Vote	F814W (mag)	K_s (mag)	F814W$-K_s$ (mag)	a_e (kpc)	n	Axial ratio	F814W$_{GALFIT}$ (mag)	χ^2_{GALFIT}
(1)	(2)	(3)	(4)	(5)	(6)	(7)	(8)	(9)	(10)	(11)	(12)
ero_141520.43+520300.8	0.92 ± 0.13	1	Secure	23.87 ± 0.08	19.82 ± 0.14	4.05	0.69 ± 0.17	6.86 ± 3.99	0.37 ± 0.12	23.50 ± 0.08	0.720
ero_141521.67+520358.0	0.97 ± 0.14	1	Secure	23.67 ± 0.03	19.66 ± 0.89	4.01	1.32 ± 0.18	1.75 ± 0.63	0.85 ± 0.16	24.13 ± 0.00	0.720
ero_141521.72+520354.2	1.04 ± 0.14	3	Unsecure	23.74 ± 0.01	18.97 ± 0.01	4.77	1.34 ± 0.19	1.75 ± 0.63	0.85 ± 0.16	24.13 ± 0.00	0.720
ero_141524.80+520419.0	0.95 ± 0.14	1	Secure	23.61 ± 0.03	19.32 ± 0.03	4.29	2.76 ± 0.35	1.70 ± 0.38	0.71 ± 0.07	23.36 ± 0.08	0.716
ero_141526.12+520555.9	1.61 ± 0.18	2c	Unsecure	24.15 ± 0.02	19.24 ± 0.03	4.91	4.66 ± 1.02	1.53 ± 0.49	0.31 ± 0.05	23.97 ± 0.14	0.709
ero_141526.29+520417.5	2.34 ± 0.23	2b	Secure	25.12 ± 0.01	20.65 ± 0.53	4.47	3.56 ± 0.35	0.33 ± 0.25	0.15 ± 0.05	24.48 ± 0.10	0.734
ero_141526.54+520258.1	1.75 ± 0.19	1	Secure	24.95 ± 0.02	20.42 ± 0.95	4.53	1.72 ± 0.41	2.58 ± 1.81	0.24 ± 0.13	24.46 ± 0.12	0.733
ero_141526.65+520405.0	0.91 ± 0.13	1	Secure	24.94 ± 0.02	20.82 ± 0.27	4.12	0.54 ± 0.14	0.13 ± 2.51	0.75 ± 0.36	24.95 ± 0.08	0.755
ero_141528.89+520415.9#	2.00 ± 0.21	1	Secure	24.49 ± 0.46	20.46 ± 0.51	4.03	0.01 ± 0.56	9.09 ± 174.96	0.99 ± 3.93	24.16 ± 12.95	0.742
ero_141530.47+520504.3	0.68 ± 0.12	2b	Secure	21.76 ± 0.00	17.73 ± 0.03	4.03	20.17 ± 1.88	1.50 ± 0.13	0.29 ± 0.01	20.55 ± 0.08	1.591
ero_141531.91+520339.0	1.52 ± 0.18	1	Unsecure	23.98 ± 0.37	19.74 ± 0.61	4.24	0.51 ± 0.07	3.29 ± 1.66	0.98 ± 0.22	23.55 ± 0.04	0.715
ero_141532.19+520438.6	1.40 ± 0.17	1	Secure	24.07 ± 0.03	20.06 ± 0.13	4.01	0.44 ± 0.26	12.81 ± 17.93	0.21 ± 0.14	23.84 ± 0.38	0.718
ero_141534.63+520303.0	2.67 ± 0.26	2b	Secure	24.99 ± 0.01	20.45 ± 0.26	4.54	2.60 ± 0.61	0.07 ± 0.60	0.40 ± 0.14	25.07 ± 0.25	1.959
ero_141541.34+520749.7	1.09 ± 0.15	3	Secure	22.75 ± 0.02	18.50 ± 0.02	4.25	10.38 ± 1.68	2.02 ± 0.28	0.66 ± 0.04	21.88 ± 0.13	0.744
ero_141541.93+520639.0	1.70 ± 0.19	1	Secure	23.52 ± 0.03	19.24 ± 0.43	4.27	1.64 ± 0.15	1.58 ± 0.47	0.46 ± 0.06	23.48 ± 0.04	0.730
ero_141542.14+520643.8	0.94 ± 0.14	2b	Secure	23.71 ± 0.01	19.43 ± 0.01	4.28	8.26 ± 0.57	0.15 ± 0.08	0.10 ± 0.04	23.71 ± 0.16	1.096
ero_141544.23+520731.9	1.09 ± 0.15	2b	Secure	24.13 ± 0.01	20.00 ± 0.01	4.13	8.34 ± 10.24	0.04 ± 0.12	0.16 ± 0.04	24.50 ± 0.00	0.776
ero_141546.60+520921.1	1.77 ± 0.19	4	Unsecure	24.87 ± 0.01	20.44 ± 0.78	4.43	3.19 ± 6.06	0.05 ± 0.48	0.29 ± 0.08	24.91 ± 0.13	0.718
ero_141547.57+520653.5	1.52 ± 0.18	2b	Secure	24.20 ± 0.02	20.15 ± 0.87	4.05	3.03 ± 0.74	2.37 ± 0.99	0.44 ± 0.09	23.88 ± 0.15	0.740
ero_141547.81+520912.0*	1.83 ± 0.20	3	Unsecure	23.15 ± 0.03	19.10 ± 0.07	4.05	30.80 ± 94.13	19.73 ± 18.08	0.22 ± 0.04	22.36 ± 0.92	0.764
ero_141550.16+520706.3	1.60 ± 0.18	2b	Secure	23.80 ± 0.01	19.44 ± 0.42	4.37	4.46 ± 0.42	0.74 ± 0.16	0.59 ± 0.04	23.44 ± 0.06	0.732
ero_141551.31+520954.3	0.97 ± 0.14	1	Secure	24.00 ± 0.03	19.73 ± 0.04	4.28	0.71 ± 0.19	5.83 ± 4.20	0.66 ± 0.17	23.73 ± 0.15	0.723
ero_141551.59+521030.1	1.06 ± 0.14	2a	Secure	23.56 ± 0.03	19.20 ± 0.02	4.36	7.25 ± 4.61	6.28 ± 2.62	0.32 ± 0.05	22.88 ± 0.29	0.727
ero_141552.93+520701.4	1.54 ± 0.18	1	Secure	23.67 ± 0.03	19.36 ± 0.54	4.31	1.75 ± 0.20	2.36 ± 0.74	0.48 ± 0.07	23.42 ± 0.06	0.736
ero_141552.95+520739.5	1.79 ± 0.20	1	Secure	24.35 ± 0.03	20.01 ± 0.16	4.34	0.86 ± 0.22	3.80 ± 2.79	0.70 ± 0.17	24.00 ± 0.13	0.764
ero_141553.33+520718.4	1.32 ± 0.16	3	Secure	23.81 ± 0.01	19.27 ± 0.02	4.55	3.08 ± 1.84	0.05 ± 0.21	0.62 ± 0.08	24.09 ± 0.09	0.808
ero_141557.80+521052.2	0.90 ± 0.13	2b	Secure	23.08 ± 0.00	18.82 ± 0.37	4.25	6.08 ± 0.43	0.82 ± 0.11	0.46 ± 0.02	22.78 ± 0.05	0.719
ero_141559.96+521057.4	0.98 ± 0.14	1	Secure	22.53 ± 0.03	18.48 ± 0.07	4.05	15.23 ± 15.24	11.11 ± 4.07	0.83 ± 0.06	21.42 ± 0.40	0.756
ero_141600.38+520846.2	1.71 ± 0.19	2b	Secure	24.26 ± 0.00	20.08 ± 0.68	4.17	4.67 ± 0.35	0.28 ± 0.14	0.37 ± 0.04	23.95 ± 0.08	0.749
ero_141600.97+520908.0	1.34 ± 0.16	2b	Secure	24.40 ± 0.02	20.21 ± 0.68	4.19	3.13 ± 0.26	0.31 ± 0.20	0.30 ± 0.04	24.24 ± 0.07	0.711
ero_141601.22+521101.4*	0.94 ± 0.14	2c	Unsecure	23.44 ± 0.03	18.97 ± 0.02	4.47	5.14 ± 0.91	2.15 ± 0.47	0.32 ± 0.03	23.13 ± 0.11	0.758
ero_141603.15+521140.8	1.05 ± 0.14	3	Secure	24.10 ± 0.00	19.20 ± 0.01	4.90	4.40 ± 7.03	0.04 ± 0.15	0.71 ± 0.10	24.21 ± 0.00	0.750
ero_141604.29+520925.9	2.74 ± 0.26	1	Secure	24.57 ± 0.02	20.29 ± 0.05	4.28	0.99 ± 0.12	0.72 ± 0.60	0.46 ± 0.10	24.32 ± 0.06	0.720
ero_141605.16+520903.5	0.90 ± 0.13	4	Secure	24.52 ± 0.01	20.41 ± 0.44	4.11	6.81 ± 3.76	3.08 ± 1.64	0.17 ± 0.04	24.02 ± 0.31	0.743
ero_141608.87+521132.3	2.35 ± 0.23	3	Unsecure	23.92 ± 0.03	19.87 ± 0.82	4.05	38.01 ± 98.69	11.70 ± 10.40	0.17 ± 0.03	22.72 ± 1.01	0.725
ero_141611.77+521316.9	1.28 ± 0.16	1	Secure	23.95 ± 0.72	19.91 ± 0.04	4.03	0.34 ± 82.83	0.02 ± 99.00	0.61 ± 99.00	24.67 ± 99.00	1.052
ero_141617.81+521413.4#	1.75 ± 0.19	1	Secure	24.14 ± 0.31	19.85 ± 0.93	4.29	0.01 ± 0.06	7.03 ± 17.23	0.79 ± 11.86	23.90 ± 0.00	0.781
ero_141620.23+521317.2	2.20 ± 0.22	2b	Secure	25.32 ± 0.01	21.17 ± 0.49	4.15	3.97 ± 0.44	0.08 ± 0.29	0.21 ± 0.05	24.83 ± 0.12	0.723
ero_141628.33+521419.3	1.80 ± 0.20	2b	Secure	24.27 ± 0.01	20.24 ± 0.19	4.03	6.52 ± 1.84	1.99 ± 0.72	0.19 ± 0.04	23.93 ± 0.18	0.704
ero_141629.52+521507.6	1.27 ± 0.16	2a	Secure	24.86 ± 0.02	20.55 ± 0.81	4.31	1.24 ± 0.17	0.85 ± 0.71	0.19 ± 0.17	24.57 ± 0.07	0.743

Table A1 – *continued*

Name	z_{phot}	Class	Vote	F814W (mag)	K_s (mag)	F814W$-K_s$ (mag)	a_e (kpc)	n	axial ratio	F814W$_{GALFIT}$ (mag)	χ^2_{GALFIT}
(1)	(2)	(3)	(4)	(5)	(6)	(7)	(8)	(9)	(10)	(11)	(12)
ero_141631.87+521739.0	0.71 ± 0.12	3	Secure	23.98 ± 0.02	19.92 ± 0.05	4.05	4.73 ± 0.41	0.64 ± 0.21	0.23 ± 0.03	23.79 ± 0.07	0.706
ero_141633.36+521639.7	2.12 ± 0.22	1	Secure	24.76 ± 0.09	19.93 ± 0.94	4.83	0.52 ± 0.12	0.69 ± 1.42	1.00 ± 0.39	24.60 ± 0.06	0.711
ero_141634.23+521722.7	1.23 ± 0.16	2c	Unsecure	23.55 ± 0.01	19.48 ± 0.45	4.08	8.44 ± 1.74	1.85 ± 0.39	0.39 ± 0.04	23.03 ± 0.15	0.712
ero_141634.75+521728.8	2.54 ± 0.25	1	Secure	24.00 ± 0.03	19.72 ± 0.96	4.27	1.14 ± 0.24	3.22 ± 1.86	0.53 ± 0.11	24.01 ± 0.11	0.738
ero_141635.74+521451.0	1.40 ± 0.17	1	Secure	23.06 ± 0.03	18.87 ± 0.08	4.19	1.24 ± 0.10	2.99 ± 0.60	0.54 ± 0.05	22.69 ± 0.03	0.709
ero_141636.32+521805.9	1.22 ± 0.16	4	Unsecure	24.86 ± 0.01	20.62 ± 0.54	4.25	2.76 ± 2.60	4.08 ± 3.73	0.99 ± 0.34	24.35 ± 0.51	0.729
ero_141636.41+521449.0	1.65 ± 0.19	2b	Secure	24.15 ± 0.02	20.01 ± 0.27	4.14	4.87 ± 0.50	0.51 ± 0.14	0.25 ± 0.03	23.81 ± 0.07	0.717
ero_141636.67+521806.8	1.35 ± 0.16	2a	Secure	23.76 ± 0.03	19.13 ± 0.67	4.63	5.32 ± 1.00	1.88 ± 0.44	0.40 ± 0.04	23.33 ± 0.12	0.731
ero_141639.57+521810.2	1.71 ± 0.19	2b	Secure	23.97 ± 0.01	19.88 ± 0.13	4.09	5.98 ± 0.24	0.16 ± 0.09	0.17 ± 0.02	23.65 ± 0.06	0.722
ero_141642.05+521601.7	1.49 ± 0.17	2b	Secure	24.08 ± 0.00	19.85 ± 0.26	4.22	9.08 ± 0.68	0.26 ± 0.11	0.23 ± 0.02	23.69 ± 0.07	0.707
ero_141642.20+521641.7	0.92 ± 0.13	2b	Secure	25.17 ± 0.01	20.25 ± 0.82	4.93	2.24 ± 0.32	0.76 ± 0.37	0.48 ± 0.09	24.55 ± 0.10	0.801
ero_141642.25+521820.2	0.90 ± 0.13	2c	Unsecure	25.28 ± 0.01	20.93 ± 0.56	4.35	1.53 ± 0.35	1.47 ± 1.09	0.62 ± 0.17	24.72 ± 0.14	0.734
ero_141643.79+521915.4	1.82 ± 0.20	1	Secure	23.96 ± 0.03	19.77 ± 0.22	4.18	2.84 ± 0.49	2.34 ± 0.72	0.50 ± 0.07	23.56 ± 0.11	0.719
ero_141644.29+521828.4	1.50 ± 0.17	2a	Secure	23.85 ± 0.03	19.66 ± 0.89	4.18	3.85 ± 1.81	4.92 ± 2.19	0.44 ± 0.08	23.34 ± 0.23	0.749
ero_141645.18+521650.7	0.67 ± 0.12	2a	Secure	22.02 ± 0.03	17.90 ± 0.51	4.12	12.25 ± 1.79	3.04 ± 0.32	0.42 ± 0.01	21.07 ± 0.10	0.721
ero_141646.01+521833.1[#]	1.47 ± 0.17	1	Secure	24.18 ± 0.30	20.02 ± 0.85	4.15	0.01 ± 0.26	12.13 ± 114.81	1.00 ± 2.45	23.69 ± 6.93	0.710
ero_141650.05+522119.6	1.29 ± 0.16	2c	Unsecure	22.98 ± 0.03	18.93 ± 0.59	4.05	3.44 ± 0.10	0.33 ± 0.06	0.43 ± 0.02	22.78 ± 0.03	0.728
ero_141650.65+521825.5[#]	1.67 ± 0.19	4	Unsecure	24.45 ± 0.44	20.07 ± 0.49	4.38	0.01 ± 0.03	8.94 ± 7.39	0.99 ± 3.79	24.13 ± 0.00	0.736
ero_141659.11+521920.7	1.25 ± 0.16	2a	Secure	23.09 ± 0.03	18.82 ± 0.03	4.28	3.22 ± 0.41	1.64 ± 0.41	0.41 ± 0.05	23.20 ± 0.08	1.049
ero_141705.04+522306.0	0.37 ± 0.10	1	Secure	22.86 ± 0.03	18.73 ± 0.02	4.13	29.96 ± 59.30	14.39 ± 7.56	0.65 ± 0.06	21.29 ± 0.74	0.708
ero_141705.15+522212.4	0.99 ± 0.14	1	Secure	22.26 ± 0.03	18.14 ± 0.03	4.12	4.48 ± 0.72	4.80 ± 0.64	0.87 ± 0.04	21.58 ± 0.08	0.698
ero_141706.84+522225.9	0.90 ± 0.13	2b	Secure	22.36 ± 0.04	18.18 ± 0.02	4.18	5.95 ± 0.42	2.35 ± 0.20	0.23 ± 0.01	21.97 ± 0.04	0.767
ero_141709.19+522135.3	1.34 ± 0.16	3	Unsecure	23.58 ± 0.07	19.57 ± 0.56	4.01	3.42 ± 0.52	1.84 ± 0.36	0.96 ± 0.09	23.16 ± 0.10	0.721
ero_141709.70+522449.3	1.55 ± 0.18	2b	Secure	23.98 ± 0.02	19.32 ± 0.68	4.65	4.93 ± 0.35	0.34 ± 0.15	0.20 ± 0.03	23.84 ± 0.07	0.729
ero_141710.62+522109.6	2.01 ± 0.21	1	Secure	23.75 ± 0.23	19.63 ± 0.55	4.12	0.17 ± 0.17	12.29 ± 16.25	0.46 ± 0.22	23.37 ± 0.35	0.721
ero_141711.42+522111.4	1.21 ± 0.15	1	Secure	24.48 ± 0.11	20.36 ± 0.51	4.12	0.67 ± 0.14	3.10 ± 2.39	0.87 ± 0.27	24.18 ± 0.10	0.725
ero_141714.03+522332.6	1.01 ± 0.14	3	Secure	22.81 ± 0.03	18.65 ± 0.15	4.16	2.97 ± 0.12	1.15 ± 0.11	0.51 ± 0.02	22.53 ± 0.02	0.694
ero_141714.14+522538.9	1.79 ± 0.20	1	Secure	24.41 ± 0.03	19.81 ± 0.14	4.60	1.44 ± 2.10	10.87 ± 11.18	0.46 ± 0.20	24.01 ± 0.33	0.747
ero_141715.09+522142.6	2.65 ± 0.26	1	Secure	24.73 ± 0.28	20.06 ± 0.58	4.67	3.45 ± 4.48	10.88 ± 11.37	0.06 ± 0.07	24.18 ± 0.45	0.723
ero_141716.69+522549.1	1.91 ± 0.20	4	Unsecure	24.71 ± 0.01	20.11 ± 0.66	4.60	0.87 ± 0.21	2.19 ± 1.97	0.48 ± 0.22	24.66 ± 0.00	1.046
ero_141721.02+522343.5	1.43 ± 0.17	1	Secure	23.44 ± 0.03	19.29 ± 0.79	4.16	1.18 ± 0.10	2.06 ± 0.56	0.46 ± 0.06	23.19 ± 0.03	0.703
ero_141722.55+522345.6	1.41 ± 0.17	1	Secure	22.33 ± 0.05	18.13 ± 0.12	4.20	0.78 ± 0.06	5.50 ± 0.93	0.86 ± 0.05	22.01 ± 0.02	0.704
ero_141723.61+522555.2[*]	1.28 ± 0.16	3	Secure	23.45 ± 0.02	18.94 ± 0.01	4.51	11.01 ± 0.63	0.23 ± 0.06	0.32 ± 0.02	23.11 ± 0.06	0.748
ero_141726.68+522415.1	1.12 ± 0.15	2a	Secure	24.12 ± 0.29	19.91 ± 0.09	4.21	3.77 ± 1.21	3.22 ± 1.33	0.29 ± 0.06	23.75 ± 0.18	0.711
ero_141726.95+522449.6[*]	1.17 ± 0.15	2b	Secure	22.99 ± 0.00	18.76 ± 0.02	4.23	11.26 ± 0.60	0.13 ± 0.08	0.12 ± 0.01	23.34 ± 0.00	0.765
ero_141727.73+522411.6	1.47 ± 0.17	2a	Secure	23.92 ± 0.03	19.66 ± 0.30	4.26	1.74 ± 0.15	1.33 ± 0.44	0.21 ± 0.06	23.66 ± 0.04	0.717
ero_141728.35+522606.0	2.35 ± 0.23	1	Secure	24.80 ± 0.03	19.75 ± 0.17	5.04	1.35 ± 0.30	1.54 ± 1.28	0.18 ± 0.19	24.79 ± 0.08	0.714
ero_141730.64+522823.8	1.27 ± 0.16	3	Unsecure	24.84 ± 0.02	20.77 ± 0.30	4.07	0.88 ± 0.32	3.52 ± 3.63	0.79 ± 0.26	24.59 ± 0.20	0.720
ero_141731.31+522507.0	2.90 ± 0.27	3	Unsecure	24.81 ± 0.50	20.79 ± 0.52	4.02	10.21 ± 20.32	5.34 ± 5.76	0.37 ± 0.14	23.91 ± 1.04	0.740
ero_141735.49+522554.4	1.45 ± 0.17	1	Secure	23.77 ± 0.13	18.92 ± 0.02	4.84	1.42 ± 0.21	3.16 ± 1.22	0.62 ± 0.07	23.48 ± 0.08	0.778

Table A1 – *continued*

Name	$z_{\rm phot}$	Class	Vote	F814W (mag)	$K_{\rm s}$ (mag)	F814W$-K_{\rm s}$ (mag)	$a_{\rm e}$ (kpc)	n	Axial ratio	F814W$_{\rm GALFIT}$ (mag)	$\chi^2_{\rm GALFIT}$
(1)	(2)	(3)	(4)	(5)	(6)	(7)	(8)	(9)	(10)	(11)	(12)
ero_141739.07+522843.8	0.91 ± 0.13	2a	Secure	23.75 ± 0.03	19.50 ± 0.03	4.25	2.05 ± 0.17	1.90 ± 0.46	0.60 ± 0.06	23.25 ± 0.06	0.720
ero_141740.22+522905.9	1.65 ± 0.19	1	Secure	24.74 ± 0.03	19.49 ± 0.03	5.25	5.16 ± 2.19	4.28 ± 1.36	0.65 ± 0.08	23.88 ± 0.23	0.930
ero_141740.84+522649.4	1.75 ± 0.19	1	Secure	24.44 ± 0.02	19.74 ± 0.03	4.71	2.24 ± 7.76	19.99 ± 46.59	1.00 ± 0.35	23.57 ± 1.25	0.702
ero_141742.38+523034.4	1.08 ± 0.15	2a	Secure	24.25 ± 0.02	19.66 ± 0.90	4.60	24.38 ± 59.47	8.71 ± 8.13	0.26 ± 0.07	23.09 ± 1.08	0.725
ero_141742.39+522811.5	0.99 ± 0.14	2b	Secure	23.61 ± 0.00	19.36 ± 0.03	4.26	9.30 ± 0.90	0.66 ± 0.13	0.29 ± 0.02	23.13 ± 0.07	0.713
ero_141744.08+522631.2[#]	1.99 ± 0.21	1	Secure	25.07 ± 0.36	20.52 ± 0.06	4.55	0.05 ± 6.60	3.15 ± 333.19	0.78 ± 9.04	24.86 ± 10.73	0.721
ero_141744.28+522925.0	0.75 ± 0.12	1	Secure	25.33 ± 0.03	20.71 ± 0.01	4.62	0.91 ± 0.23	3.57 ± 2.43	0.67 ± 0.18	25.15 ± 0.14	0.936
ero_141745.13+523045.9	1.40 ± 0.17	4	Unsecure	25.02 ± 0.00	20.83 ± 0.52	4.19	3.50 ± 0.72	0.99 ± 0.34	0.50 ± 0.09	24.35 ± 0.14	0.733
ero_141746.71+522857.8	1.59 ± 0.18	2b	Secure	25.43 ± 0.02	21.18 ± 0.02	4.26	2.58 ± 0.22	0.29 ± 0.19	0.53 ± 0.05	25.19 ± 0.07	0.924
ero_141749.11+522759.6	0.93 ± 0.14	1	Secure	24.26 ± 0.06	20.22 ± 0.01	4.04	0.91 ± 0.09	2.15 ± 0.68	0.52 ± 0.06	24.15 ± 0.03	1.071
ero_141749.24+522811.0	1.08 ± 0.15	3	Secure	23.11 ± 0.16	19.04 ± 0.03	4.08	1.65 ± 0.10	5.70 ± 0.69	0.39 ± 0.04	23.11 ± 0.00	1.255
ero_141749.59+522806.2	1.51 ± 0.18	2b	Secure	24.34 ± 0.03	20.16 ± 0.03	4.19	4.46 ± 0.30	0.62 ± 0.16	0.28 ± 0.02	24.11 ± 0.05	1.371
ero_141751.29+523040.3	1.51 ± 0.18	2a	Secure	23.84 ± 0.03	19.65 ± 0.81	4.19	2.73 ± 0.26	1.15 ± 0.21	0.73 ± 0.06	23.49 ± 0.06	0.710
ero_141751.38+523049.8	1.54 ± 0.18	3	Secure	24.88 ± 0.01	19.79 ± 0.47	5.09	4.94 ± 0.34	0.16 ± 0.15	0.23 ± 0.04	24.34 ± 0.09	0.712
ero_141751.76+523136.8	1.33 ± 0.16	2a	Secure	23.26 ± 0.03	18.54 ± 0.08	4.72	3.16 ± 0.44	2.48 ± 0.50	0.73 ± 0.06	22.93 ± 0.09	0.716
ero_141754.50+523023.4	4.60 ± 0.39	1	Secure	24.93 ± 0.23	20.46 ± 0.46	4.47	0.35 ± 0.19	6.95 ± 12.99	0.78 ± 0.51	24.61 ± 0.37	0.723
ero_141755.44+522928.5	2.98 ± 0.28	4	Unsecure	24.70 ± 0.04	20.43 ± 0.62	4.27	0.81 ± 0.11	1.26 ± 1.10	0.22 ± 0.16	24.47 ± 0.07	0.708
ero_141756.74+523157.2	1.32 ± 0.16	2c	Unsecure	23.04 ± 0.03	18.64 ± 0.14	4.40	4.92 ± 0.51	1.33 ± 0.17	0.65 ± 0.04	22.87 ± 0.07	0.726
ero_141756.91+523118.1	1.48 ± 0.17	4	Unsecure	24.29 ± 0.01	20.24 ± 0.47	4.04	2.72 ± 3.11	6.12 ± 6.92	0.54 ± 0.20	24.31 ± 0.54	0.718
ero_141757.15+523242.6	1.61 ± 0.18	1	Secure	24.27 ± 0.07	19.69 ± 0.16	4.58	0.80 ± 0.29	6.34 ± 5.66	0.47 ± 0.20	24.14 ± 0.14	0.721
ero_141757.27+523224.5[#]	1.34 ± 0.16	1	Secure	24.29 ± 0.60	19.49 ± 0.71	4.80	0.01 ± 17.87	4.81 ± 3912.27	0.83 ± 119.26	24.00 ± 738.06	0.719
ero_141757.66+522910.3	1.33 ± 0.16	2b	Secure	24.04 ± 0.00	19.85 ± 0.00	4.19	4.48 ± 1.55	2.30 ± 0.86	0.56 ± 0.10	23.68 ± 0.22	0.739
ero_141800.87+523203.0	1.59 ± 0.18	2a	Secure	23.93 ± 0.03	19.07 ± 0.03	4.86	2.07 ± 0.36	2.96 ± 1.00	0.81 ± 0.08	23.42 ± 0.11	0.720
ero_141802.03+523015.5	1.64 ± 0.18	2b	Secure	24.05 ± 0.03	19.70 ± 0.08	4.35	2.69 ± 0.17	0.07 ± 0.32	0.29 ± 0.05	24.41 ± 0.08	0.711
ero_141802.57+523251.8	1.73 ± 0.19	4	Unsecure	25.00 ± 0.01	19.86 ± 0.59	5.14	5.82 ± 2.04	1.56 ± 0.78	0.18 ± 0.05	24.52 ± 0.22	0.719
ero_141803.00+523033.9	1.35 ± 0.16	4	Unsecure	24.97 ± 0.01	20.92 ± 0.49	4.05	1.21 ± 0.34	0.11 ± 1.06	0.85 ± 0.21	24.81 ± 0.08	0.736
ero_141803.34+523228.4	1.10 ± 0.15	1	Secure	24.62 ± 0.08	19.97 ± 0.52	4.65	1.21 ± 0.54	7.08 ± 6.38	0.08 ± 0.12	24.29 ± 0.18	0.717
ero_141809.26+523112.5	0.84 ± 0.13	2b	Secure	23.46 ± 0.02	19.19 ± 0.01	4.27	6.68 ± 0.54	1.10 ± 0.17	0.20 ± 0.01	22.94 ± 0.05	0.726

Table A2. Results of mass and age analysis : (2) formation redshift z_f, (3) exponential decay time τ, (4) optical depth A_v, (5) metallicity Z, (6) luminosity distance D_L, (7) total stellar mass M_{tot}, (8) age, (9) χ^2.

Name	z_f	τ (Gyr)	A_v	Z	D_L/ 10^3 Mpc	M_{tot}/ 10^{10} $M_\odot$	Age/ 10^8 yr	χ^2
(1)	(2)	(3)	(4)	(5)	(6)	(7)	(8)	(9)
ero_141520.43+520300.8	3	7.00	2.0	0.004	$5.92^{+1.05}_{-1.09}$	2.216	18.000	0.45
ero_141521.67+520358.0	3	0.50	1.0	0.008	$6.40^{+1.10}_{-1.14}$	3.690	21.000	1.04
ero_141521.72+520354.2	4	0.50	1.0	0.020	$6.94^{+1.16}_{-1.20}$	11.596	23.000	3.13
ero_141524.80+520419.0	5	1.00	0.6	0.050	$6.20^{+1.08}_{-1.12}$	8.735	45.000	5.92
ero_141526.12+520555.9	3	0.05	0.6	0.050	$11.95^{+1.65}_{-1.69}$	32.103	10.150	28.18
ero_141526.29+520417.5	8	4.00	0.6	0.004	$18.82^{+2.27}_{-2.31}$	2.575	21.000	39.75
ero_141526.54+520258.1	3	0.05	0.6	0.050	$13.19^{+1.76}_{-1.80}$	8.471	5.088	16.25
ero_141526.65+520405.0	3	0.10	2.0	0.020	$5.84^{+1.04}_{-1.08}$	0.781	4.535	12.43
ero_141528.89+520415.9	3	0.10	0.6	0.050	$15.49^{+1.97}_{-2.01}$	6.118	4.535	1.33
ero_141530.47+520504.3	3	0.50	2.0	0.020	$4.11^{+0.85}_{-0.89}$	12.818	12.780	1.78
ero_141531.91+520339.0	3	0.05	1.0	0.050	$11.13^{+1.57}_{-1.61}$	6.340	3.210	1.53
ero_141532.19+520438.6	3	0.10	0.6	0.050	$10.02^{+1.46}_{-1.50}$	5.981	6.405	3.36
ero_141534.63+520303.0	6	0.50	1.0	0.008	$22.09^{+2.55}_{-2.59}$	16.444	12.780	7.02
ero_141541.34+520749.7	4	0.05	1.0	0.050	$7.39^{+1.20}_{-1.24}$	2.473	1.805	42.22
ero_141541.93+520639.0	3	0.05	0.6	0.050	$12.68^{+1.72}_{-1.76}$	23.354	5.088	20.08
ero_141542.14+520643.8	3	0.10	2.0	0.050	$6.08^{+1.07}_{-1.11}$	2.988	4.042	3.00
ero_141544.23+520731.9	8	1.00	0.6	0.008	$7.35^{+1.20}_{-1.24}$	7.365	47.500	1.79
ero_141546.60+520921.1	4	0.50	0.6	0.004	$13.42^{+1.78}_{-1.82}$	4.458	16.090	8.64
ero_141547.57+520653.5	6	1.00	0.6	0.004	$11.13^{+1.57}_{-1.61}$	9.129	30.000	8.72
ero_141547.81+520912.0	4	0.05	0.6	0.050	$13.94^{+1.83}_{-1.87}$	12.119	2.861	5.97
ero_141550.16+520706.3	3	0.10	0.6	0.050	$11.81^{+1.64}_{-1.67}$	18.843	7.187	8.84
ero_141551.31+520954.3	3	0.10	2.0	0.020	$6.36^{+1.10}_{-1.14}$	2.688	4.535	5.68
ero_141551.59+521030.1	3	0.50	1.0	0.020	$7.14^{+1.18}_{-1.22}$	5.610	16.800	3.00
ero_141552.93+520701.4	3	0.10	0.6	0.050	$11.31^{+1.59}_{-1.63}$	10.474	5.709	7.64
ero_141552.95+520739.5	5	1.00	1.0	0.050	$13.61^{+1.80}_{-1.84}$	18.458	21.000	1.20
ero_141553.33+520718.4	4	0.50	0.6	0.004	$9.36^{+1.40}_{-1.44}$	10.254	27.500	12.49
ero_141557.80+521052.2	3	0.05	2.0	0.004	$5.76^{+1.03}_{-1.07}$	3.210	3.602	2.41
ero_141559.96+521057.4	3	0.05	1.0	0.050	$6.49^{+1.11}_{-1.15}$	8.592	6.405	9.32
ero_141600.38+520846.2	5	1.00	0.6	0.004	$12.82^{+1.73}_{-1.77}$	7.748	23.000	0.47
ero_141600.97+520908.0	3	0.10	0.6	0.050	$9.53^{+1.42}_{-1.46}$	3.119	5.088	0.65
ero_141601.22+521101.4	3	0.50	1.0	0.020	$6.16^{+1.08}_{-1.12}$	8.560	24.000	0.67
ero_141603.15+521140.8	4	0.50	0.6	0.050	$7.06^{+1.17}_{-1.21}$	8.658	27.500	1.62
ero_141604.29+520925.9	7	1.00	0.6	0.004	$22.79^{+2.61}_{-2.65}$	8.224	14.340	8.32
ero_141605.16+520903.5	–	–	–	–	$5.76^{+1.03}_{-1.07}$	–	–	–
ero_141608.87+521132.3	4	0.05	0.6	0.008	$18.87^{+2.27}_{-2.31}$	7.863	2.550	2.36
ero_141611.77+521316.9	3	0.10	0.6	0.050	$9.01^{+1.37}_{-1.41}$	5.529	7.187	4.97
ero_141617.81+521413.4	3	0.05	0.6	0.050	$13.24^{+1.77}_{-1.81}$	14.111	4.535	21.89
ero_141620.23+521317.2	5	0.50	0.6	0.004	$17.46^{+2.15}_{-2.19}$	5.069	14.340	6.35
ero_141628.33+521419.3	3	0.05	0.6	0.008	$13.70^{+1.81}_{-1.85}$	4.239	4.042	3.27
ero_141629.52+521507.6	3	0.10	0.6	0.050	$8.88^{+1.35}_{-1.39}$	2.272	7.187	9.82
ero_141631.87+521739.0	4	1.00	0.6	0.050	$4.33^{+0.87}_{-0.91}$	1.683	40.000	1.17
ero_141633.36+521639.7	3	0.05	3.0	0.008	$16.64^{+2.07}_{-2.11}$	26.603	0.905	5.54
ero_141634.23+521722.7	3	0.50	0.6	0.020	$8.54^{+1.32}_{-1.36}$	5.580	16.090	3.45
ero_141634.75+521728.8	4	0.10	1.0	0.008	$20.84^{+2.44}_{-2.48}$	28.976	4.535	0.21
ero_141635.74+521451.0	3	0.05	0.6	0.050	$9.97^{+1.46}_{-1.50}$	18.914	6.405	23.77

Table A2 – *continued*

Name	z_f	τ (Gyr)	A_v	Z	D_L/ 10^3 Mpc	M_{tot}/ 10^{10} $M_\odot$	Age/ 10^8 yr	χ^2
(1)	(2)	(3)	(4)	(5)	(6)	(7)	(8)	(9)
ero_141636.32+521805.9	5	1.00	0.6	0.020	$8.45^{+1.31}_{-1.35}$	3.656	35.000	2.26
ero_141636.41+521449.0	3	0.05	0.6	0.050	$12.27^{+1.68}_{-1.72}$	11.295	5.088	14.06
ero_141636.67+521806.8	4	0.50	0.6	0.004	$9.62^{+1.43}_{-1.47}$	15.017	30.000	3.09
ero_141639.57+521810.2	3	0.10	0.6	0.004	$12.78^{+1.73}_{-1.76}$	3.340	4.042	0.28
ero_141642.05+521601.7	3	0.10	0.6	0.050	$10.82^{+1.54}_{-1.58}$	9.549	7.187	7.50
ero_141642.20+521641.7	3	0.10	2.0	0.050	$5.92^{+1.05}_{-1.09}$	1.086	4.535	12.90
ero_141642.25+521820.2	–	–	–	–	$5.80^{+1.04}_{-1.08}$	–	–	–
ero_141643.79+521915.4	3	0.10	2.0	0.050	$13.84^{+1.82}_{-1.86}$	17.196	2.273	0.52
ero_141644.29+521828.4	3	0.05	0.6	0.008	$10.91^{+1.55}_{-1.59}$	5.097	5.088	0.30
ero_141645.18+521650.7	3	0.50	2.0	0.004	$4.04^{+0.84}_{-0.88}$	12.094	22.000	0.32
ero_141646.01+521833.1	3	0.05	0.6	0.050	$10.64^{+1.52}_{-1.56}$	14.935	10.150	125.76
ero_141650.05+522119.6	3	0.05	0.6	0.050	$9.10^{+1.38}_{-1.41}$	10.042	5.088	7.84
ero_141650.65+521825.5	4	0.10	0.6	0.004	$12.45^{+1.70}_{-1.73}$	7.379	9.048	9.01
ero_141659.11+521920.7	3	0.05	0.6	0.004	$8.71^{+1.34}_{-1.38}$	9.050	11.390	3.01
ero_141705.04+522306.0	3	2.00	2.0	0.020	$1.98^{+0.58}_{-0.62}$	2.888	70.000	3.37
ero_141705.15+522212.4	3	0.10	2.0	0.008	$6.57^{+1.12}_{-1.16}$	16.754	5.088	16.63
ero_141706.84+522225.9	3	0.10	2.0	0.020	$5.76^{+1.03}_{-1.07}$	8.713	4.535	6.68
ero_141709.19+522135.3	4	0.10	0.6	0.020	$9.53^{+1.42}_{-1.46}$	6.695	7.187	1.41
ero_141709.70+522449.3	4	0.50	0.6	0.020	$11.41^{+1.60}_{-1.64}$	17.260	21.000	1.14
ero_141710.62+522109.6	3	7.00	2.0	0.050	$15.63^{+1.99}_{-2.02}$	7.967	1.805	11.11
ero_141711.42+522111.4	6	1.00	0.6	0.008	$8.37^{+1.30}_{-1.34}$	5.265	40.000	1.65
ero_141714.03+522332.6	6	1.00	0.6	0.008	$6.73^{+1.14}_{-1.18}$	18.328	47.500	4.06
ero_141714.14+522538.9	3	0.10	0.6	0.050	$13.61^{+1.80}_{-1.84}$	16.819	7.187	14.47
ero_141715.09+522142.6	7	0.50	1.0	0.004	$21.84^{+2.53}_{-2.57}$	31.400	16.090	5.68
ero_141716.69+522549.1	6	1.00	1.0	0.004	$14.69^{+1.90}_{-1.94}$	14.913	23.000	2.68
ero_141721.02+522343.5	3	0.05	1.0	0.050	$10.28^{+1.49}_{-1.53}$	8.020	3.210	1.14
ero_141722.55+522345.6	3	0.05	0.6	0.020	$10.06^{+1.47}_{-1.51}$	28.027	6.405	3.96
ero_141723.61+522555.2	4	0.10	0.6	0.050	$9.01^{+1.37}_{-1.41}$	8.897	6.405	4.12
ero_141726.68+522415.1	5	1.00	1.0	0.004	$7.60^{+1.23}_{-1.27}$	7.882	40.000	2.70
ero_141726.95+522449.6	3	0.05	1.0	0.020	$8.02^{+1.27}_{-1.31}$	12.238	6.405	1.32
ero_141727.73+522411.6	3	0.05	0.6	0.050	$10.60^{+1.52}_{-1.56}$	16.332	9.048	77.89
ero_141728.35+522606.0	4	0.10	0.6	0.050	$18.92^{+2.28}_{-2.32}$	32.707	6.405	2.68
ero_141730.64+522823.8	4	0.05	1.0	0.050	$8.88^{+1.35}_{-1.39}$	1.711	3.602	7.15
ero_141731.31+522507.0	6	0.50	0.6	0.004	$24.41^{+2.75}_{-2.79}$	8.577	11.390	21.13
ero_141735.49+522554.4	6	0.50	0.6	0.020	$10.46^{+1.51}_{-1.55}$	47.326	32.500	13.43
ero_141739.07+522843.8	4	1.00	0.6	0.050	$5.88^{+1.05}_{-1.09}$	7.750	45.000	0.08
ero_141740.22+522905.9	4	0.05	0.6	0.020	$12.27^{+1.68}_{-1.72}$	26.014	20.000	21.29
ero_141740.84+522649.4	3	0.05	1.0	0.050	$13.24^{+1.77}_{-1.81}$	11.417	3.602	3.72
ero_141742.38+523034.4	3	0.50	0.6	0.050	$7.27^{+1.19}_{-1.23}$	5.637	25.000	5.11
ero_141742.39+522811.5	3	1.00	0.6	0.020	$6.53^{+1.11}_{-1.15}$	5.522	35.000	1.00
ero_141744.08+522631.2	3	0.10	0.6	0.050	$15.40^{+1.96}_{-2.00}$	6.521	5.088	1.80
ero_141744.28+522925.0	3	7.00	0.6	0.050	$4.64^{+0.91}_{-0.95}$	0.131	37.500	10.83
ero_141745.13+523045.9	4	0.50	0.6	0.050	$10.02^{+1.46}_{-1.50}$	4.447	18.000	1.46

Table A2 – *continued*

Name	z_f	τ (Gyr)	A_v	Z	D_L/ 10^3 Mpc	M_{tot}/ 10^{10} $M_\odot$	Age/ 10^8 yr	χ^2
(1)	(2)	(3)	(4)	(5)	(6)	(7)	(8)	(9)
ero_141746.71+522857.8	4	0.50	0.6	0.050	$11.77^{+1.63}_{-1.67}$	8.992	23.000	3.39
ero_141749.11+522759.6	6	1.00	1.0	0.050	$6.04^{+1.06}_{-1.10}$	7.208	50.000	8.95
ero_141749.24+522811.0	5	1.00	0.6	0.008	$7.31^{+1.20}_{-1.24}$	13.825	42.500	0.73
ero_141749.59+522806.2	5	0.50	0.6	0.050	$11.00^{+1.56}_{-1.60}$	48.593	30.000	1.70
ero_141751.29+523040.3	3	0.05	0.6	0.004	$11.00^{+1.56}_{-1.60}$	5.025	6.405	8.02
ero_141751.38+523049.8	4	0.10	0.6	0.050	$11.31^{+1.59}_{-1.63}$	20.260	16.090	32.35
ero_141751.76+523136.8	3	0.10	0.6	0.050	$9.40^{+1.41}_{-1.44}$	27.221	11.390	18.94
ero_141754.50+523023.4	–	–	–	–	$42.29^{+4.22}_{-4.27}$	–	–	-
ero_141755.44+522928.5	4	7.00	0.6	0.004	$25.17^{+2.81}_{-2.85}$	1.144	3.602	18.40
ero_141756.74+523157.2	3	0.05	0.6	0.004	$9.36^{+1.40}_{-1.44}$	11.389	11.390	2.64
ero_141756.91+523118.1	–	–	–	–	$10.73^{+1.53}_{-1.57}$	–	–	–
ero_141757.15+523242.6	3	0.05	1.0	0.050	$11.90^{+1.64}_{-1.68}$	8.622	3.602	2.93
ero_141757.27+523224.5	7	0.50	0.6	0.020	$9.49^{+1.41}_{-1.45}$	29.389	37.500	15.33
ero_141757.66+522910.3	3	0.05	0.6	0.004	$9.40^{+1.41}_{-1.44}$	1.768	3.602	2.56
ero_141800.87+523203.0	3	0.05	0.6	0.050	$11.77^{+1.63}_{-1.67}$	27.766	8.064	16.26
ero_141802.03+523015.5	–	–	–	–	$12.18^{+1.67}_{-1.71}$	–	–	–
ero_141802.57+523251.8	4	0.50	0.6	0.050	$12.96^{+1.74}_{-1.78}$	12.385	20.000	2.95
ero_141803.00+523033.9	4	0.50	0.6	0.020	$9.62^{+1.43}_{-1.47}$	2.889	16.800	1.33
ero_141803.34+523228.4	4	1.00	1.0	0.020	$7.48^{+1.21}_{-1.25}$	6.106	32.500	0.39
ero_141809.26+523112.5	6	1.00	0.6	0.050	$5.37^{+0.99}_{-1.03}$	10.680	55.000	1.14

This paper has been typeset from a TEX/LATEX file prepared by the author.